nature portfolio

https://doi.org/10.1038/s41586-025-09855-6

Supplementary information

Earliest evidence of making fire

In the format provided by the authors and unedited

Supplementary Information Guide

Earliest Evidence of Making Fire: Supplementary Information

1. Artefacts

Rob Davis, Claire Lucas, Jordan Mansfield

The palaeosol (unit 6) in Area I has been excavated over two periods of fieldwork, producing a total of 43 artefacts, all of which have been examined for macroscopic heat alteration, specifically reddening, crazing of the surface and spalling. The excavation of 1989-1993 of Area I (now designated Area I West) uncovered c. 60 m^2 of palaeosol and recovered just nine artefacts, including a handaxe, none of which are heated[1]. Recent fieldwork (2021-2024) has excavated c. 24 m^2 of palaeosol in Area I East. By contrast, 34 artefacts, including four handaxes, have been recovered of which 26 (76%) are heated (Table 1.1; Fig. 1.1).

Table 1.1. Summary of artefact quantities from palaeosol (unit 6) in Area I with those displaying macroscopic heat alterations (cracking/crazing, reddening, spalling) in brackets.

Type	Area I East	Area I West
Flake (heated)	27 (19)	6 (0)
Retouched flake (heated)	0	1 (0)
Core (heated)	1 (1)	1 (0)
Handaxe (heated)	4 (4)	1 (0)
Miscellaneous (heated)	2 (2)	0

Figure 1.1. Heated sediment in Area I East under excavation in 2023, showing section B-B' which is 50 cm in length.

2. Pyrite

Silvia Bello, Jens Najorka and Simon Parfitt

2.1 Surface features of the pyrite pseudomorphs

Methods. High-resolution 3D imaging of surface features was conducted using a focus variation microscope (Alicona InfiniteFocus G5+) with a 4× lens. Imaging parameters included a working distance of 17.5 mm and a vertical resolution of 100 nm. Complementary surface detail was captured using a JEOL IT500 scanning electron microscope (SEM) operated in variable pressure mode (~70 Pa chamber pressure).

Results. The pyrite pseudomorphs were examined microscopically to assess potential surface alterations. Although the chemical composition of the fragments had changed due to complete oxidation of the original minerals[2], their external morphology remained well preserved. Features such as polishing, edge rounding, and fine surface scratching were observed. The preservation of the original pyrite structure and surface features is particularly noteworthy, given pyrite's well-documented tendency to degrade into brittle, cracked fragments accompanied by a loss of surface luster[2]. No such signs of deterioration were observed on the two fragments from Barnham.

Specimen 2977 (Fig. 2.1a-e). This fragment exhibits a conical shape (approximately 12 × 8 × 11 mm) and corresponds to what has been described as a "fragment of a nodule of radiating pyrite" (cf. Fig. 4 in Larkin[3]). The exterior cortical surface is relatively featureless, slightly curved (Fig. 2.1a–d), and polished. Aside from a series of small indentations (Fig. 2.1d), possibly resulting from chemical alteration, this surface shows no obvious cracks, scratches, or other alterations. The internal portion of the fragment exposes the radiating crystalline structure typical of pyrite (Fig. 2.1a–b, e). The polished appearance extends to the fracture edges, which are particularly rounded and worn (Fig. 2.1e), suggesting a more prolonged surface exposure to weathering or abrasion.

Specimen 3818 (Fig. 2.2a–g). This larger fragment of pyrite pseudomorph exhibits an irregular cuboid shape, approximately 19 × 15 × 8 mm in size. It preserves portions of the exterior cortical surface, along with internal faces where the original crystalline structure typical of pyrite nodules has degraded and a reddish coloration is present (Fig. 2.2b). No surface features indicative of anthropogenic modification were identified. The edges at the junction between the cortical and internal zones display variable morphology: some are sharp and angular (Figure 2.2i), while others are polished and rounded (Fig. 2.2h-j). This edge roundness and overall polished appearance may result from a combination of chemical degradation processes, as well as weathering and sedimentary abrasion during burial.

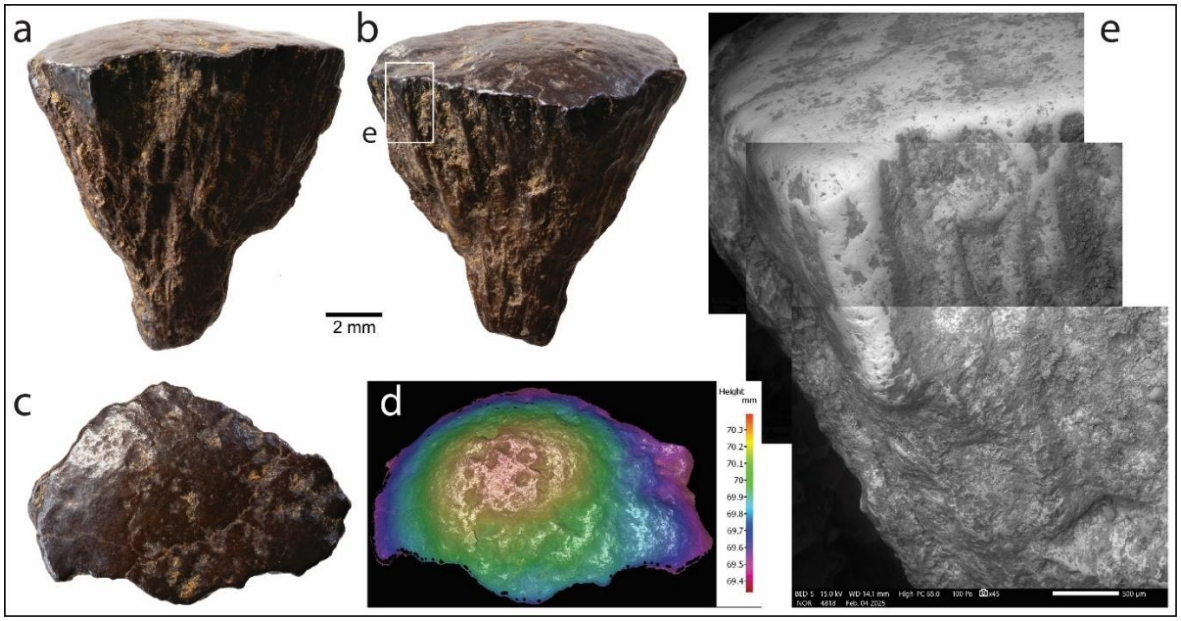

Figure 2.1. Pyrite pseudomorph specimen 2977. (**a–b**) Photographs of fracture surfaces; (**c**) external cortical surface; (**d**) hypsometrically tinted focus variation microscope image of the cortical surface showing pits. (**e**) Composite scanning electron microscope images showing polishing on the cortical surface, break edges, and exposed prominences of the crystal structure along the fractured face.

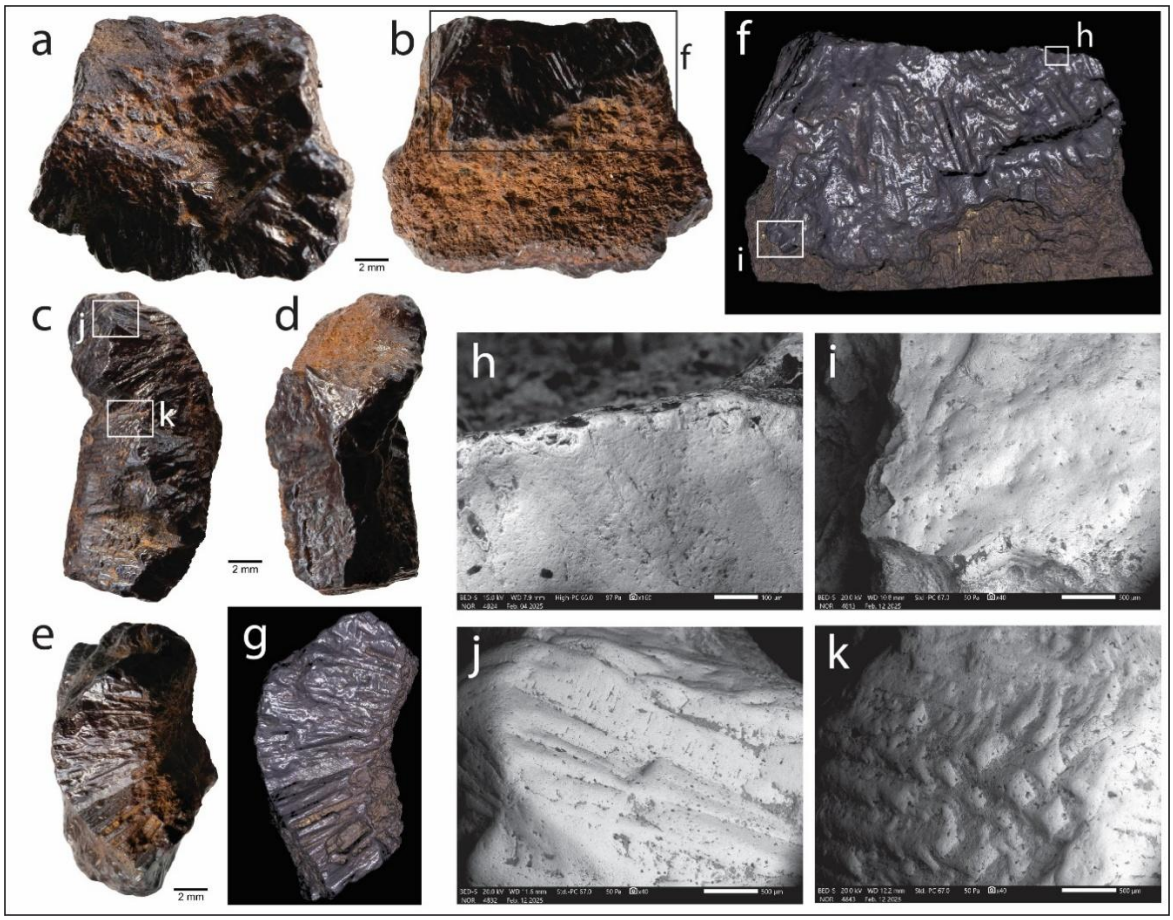

Figure 2.2. Pyrite pseudomorph specimen 3818. (**a–e**) Photographs and (**f–g**) focus variation microscope images of fracture surfaces; (**h–k**) textural features of the oxidised pyrite fragment observed under the scanning electron microscope.

2.2 XRD Analysis

A Rigaku Dmax Rapid II Micro-diffraction system (µXRD) was used to collect diffraction data from the two nodule fragments found in Areas IV(6) and VI. The analysis utilised a copper X-ray source operating at 40 kV and 36 mA, along with an incident beam monochromator, a 300 µm collimator, and a 2D curved imaging plate detector. Several point analyses were collected on the outer cortical surfaces and internal fracture faces of each nodule fragment.

The data collection targeted both flat and protruding areas, with measurements taken at a constant X-ray beam incident angle of 20° 2Theta and a maximum spot size of about 900 µm. The complete diffraction angle range from 20° to 90° 2Theta was captured. The 2D diffraction images were subsequently converted into 1D diffraction patterns using the 2DP software from Rigaku. The peak positions in the converted 1D patterns were identified by comparing them to the reference database PDF-5+ from the International Centre for Diffraction Data (ICDD), using the Highscore software from Malvern Panalytical.

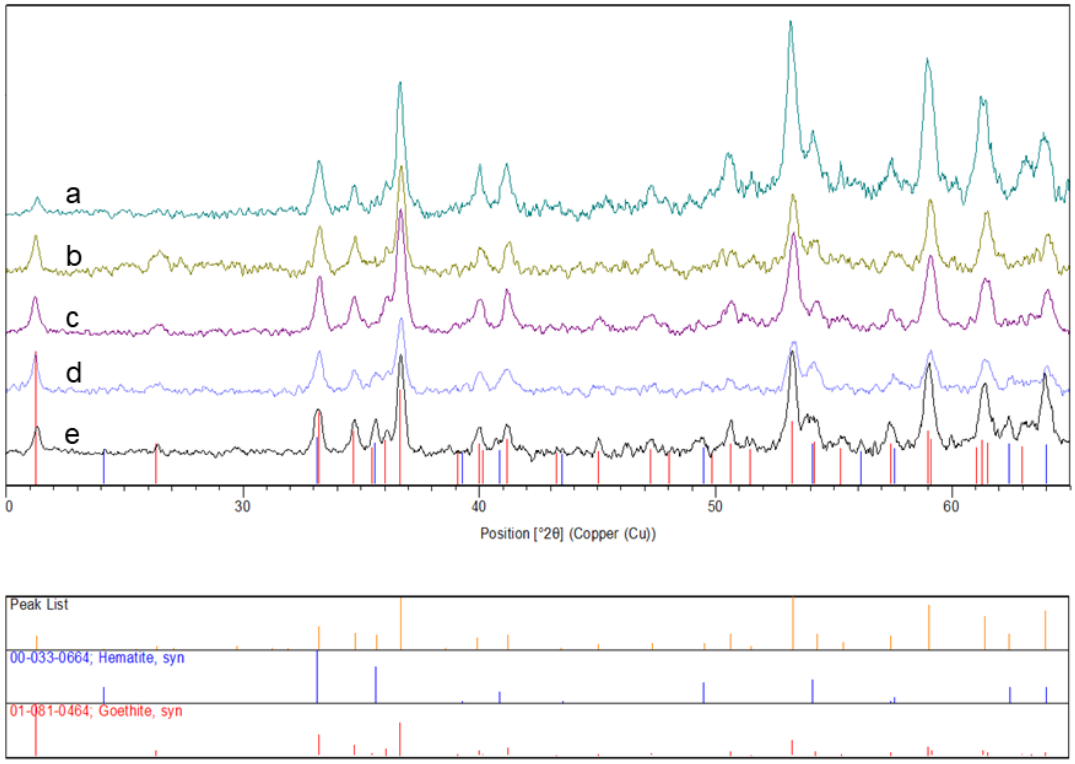

Figure 2.3. XRD patterns of the two nodule fragments of oxidised pyrite. Goethite (FeOOH) and minor haematite (Fe_2O_3) were identified indicating complete oxidation. The spot analyses are from the fragment from Area VI, (**a**) cortical surface, (**b**) interior fractured side, (**c**) radial centre, and from Area IV(6), (**d**) cortical surface and (**e**) strongly altered interior fractured side.

Nodule Mineralogy and Texture. µXRD analyses showed that goethite (FeOOH) is the main mineral phase in all measured areas, with minor haematite (Fe_2O_3) detected in some spots (Fig. 2.3). No pyrite (FeS_2) or other sulphide minerals were found, confirming that both nodule fragments are fully oxidized. Despite this, the preserved morphology of the nodule fragments is consistent with pseudomorphic replacement of radial-grown pyrite. The first fragment from Area VI has a well-preserved radial texture, characterised by elongated crystals that radiate from a central point (Fig. 2.4a). The second fragment from Area IV(6) is more heterogeneous, consisting mostly of intersecting

domains of subparallel prismatic crystals without a distinct nucleation centre. One partial radial structure is well preserved (Fig. 2.4b). Crystal shapes near to the cortex have polygonal terminations (e.g. square outlines, Fig. 2.4c), while longitudinal crystal faces show aligned rectangular outlines (Fig. 2.4b), consistent with the crystal habit of radially formed pyrite. Although a marcasite precursor cannot be entirely excluded, the presence of square and polygonal crystal terminations at the outer margin supports pyrite as the more likely original FeS_2 polymorph. It should be noted that marcasite can also produce strong sparks when struck. The innermost part of the second fragment shows a higher degree of alteration, characterised by a porous goethite matrix and a less preserved framework of relict goethite crystals.

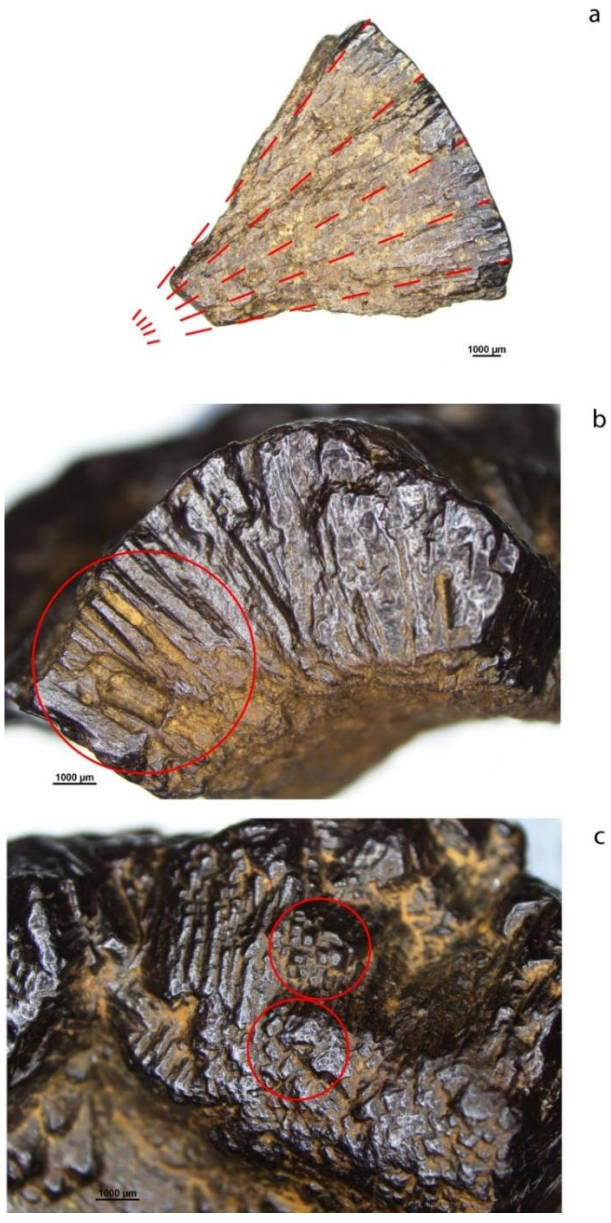

Figure 2.4. Textural features of the oxidised pyrite nodules showing the pseudomorphic replacement of radially grown pyrite to goethite. (**a**) Dashed lines on the pyrite fragment from Area VI show the radial growth schematically. (**b**) Circle on the fragment of Area IV(6) shows well preserved elongated crystals with rectangular outlines of a partial radial structure. (**c**) Areas of heterogeneous growth of the fragment from Area IV(6) with subparallel crystal domains intersecting in different orientations. Circles show areas with polygonal termination of crystals.

3. Geological Studies

3.1 Stratigraphy and chronology

Simon Lewis, Nick Ashton, Rob Davis, Mark Lewis, Simon Parfitt and Sylvia Peglar

Fieldwork from 1989-1994 and from 2013[1,4] has established that Pleistocene deposits occupy a glacial meltwater channel cut into Chalk bedrock and initially infilled with till (unit 1), sands and gravels (unit 2) and debris flow diamictons (unit 3). These are overlain by mainly fine-grained sediments, with lateral variations between the centre and the margins of the basin. At the edge of the basin these glacial deposits are overlain by a coarse lag gravel (unit 4), silty sand (unit 5e), black clay (unit 6) and brown silty clay ('brickearth', unit 7), all of which are decalcified.

Micromorphological analysis has indicated that unit 6 is a palaeosol, and a series of darker grey zones within unit 7 are interpreted as less distinct palaeosols[5]. The gravel (unit 4) thins out and the silty sand (unit 5e) thickens towards the centre of the basin, where it is calcareous, contains organic remains and is referred to as unit 5c. Pollen, molluscs and vertebrates preserved in these sediments suggest a slow-moving to still body of water that gradually dried out, surrounded by grass and deciduous vegetation with slightly warmer summers than present[6]. The drying out of the basin was followed by soil formation (unit 6) succeeded by further infilling of the basin with brown silty clay (unit 7) predominantly deposited as colluvium from the valley slopes.

The interglacial deposits (units 4 to 6) can be attributed to MIS 11 on the basis of their stratigraphic position above Anglian (MIS 12) glacial till[7], aminostratigraphy supporting attribution to MIS 11[8], and ESR on quartz ages of 448 ± 55 and 393 ± 83[9]. The mammalian fauna is typical of the Hoxnian interglacial (MIS 11c). The fauna includes the small mole (*Talpa minor*), pine vole (*Microtus* (*Terricola*) cf. *subterraneus*) and rabbit (*Oryctolagus* cf. *cuniculus*), all of which appear to be absent in Britain after MIS 11, while large fallow deer (*Dama dama*) is also typical of Hoxnian faunas[10]. The palynology of unit 5c suggests attribution to the first half of an interglacial[11], and more recent work indicates attribution to Hoxnian pollen zones I and II. Soil formation (unit 6) is likely to have started in Hoxnian pollen zone III. Molluscan biostratigraphy also supports an age in the first half of the Hoxnian interglacial with the predominance of *Discus ruderatus* over *Discus rotundatus*[8].

3.2. Sediment description of unit 6

Marcus Hatch and Simon Lewis

Subsamples of the sampling column through the palaeosol complex (unit 6) in Area I East were taken for particle size analysis (PSA) using a using a Bettersizer S3 Plus Particle Size Analyser to provide laboratory descriptions (Figs 3.1, 3.2)[12]. The results of the PSA indicate some variation in grain size, particularly in the proportion of sand (Fig. 3.3). The textural and colour characteristics provide the following subunit descriptions from bottom to top: brown clayey silt (BCS); lower black clayey silt (LBCS); yellowish-brown clayey silt (YBCS); reddened clayey silt (RCS); upper black clayey silt (UBCS).

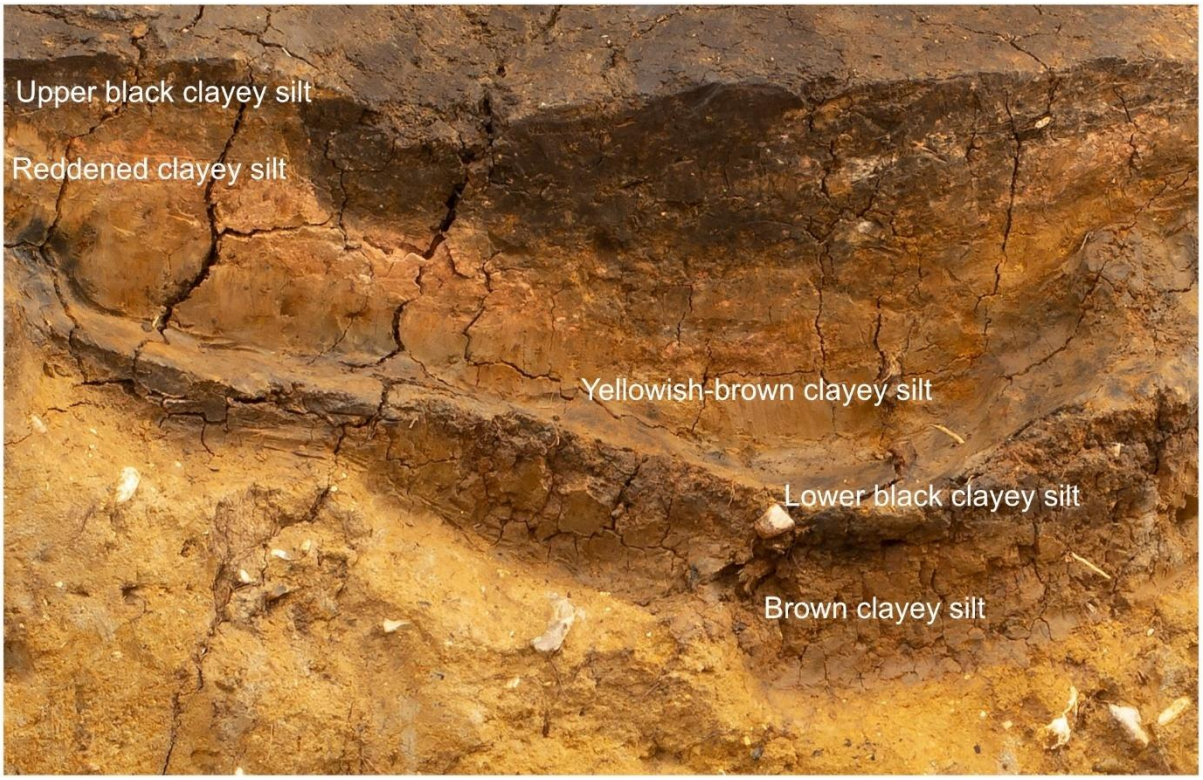

Figure 3.1. Location of sample column in Area I East with formal terms for the subunits of the palaeosol (unit 6). See Figure 3.2 for location.

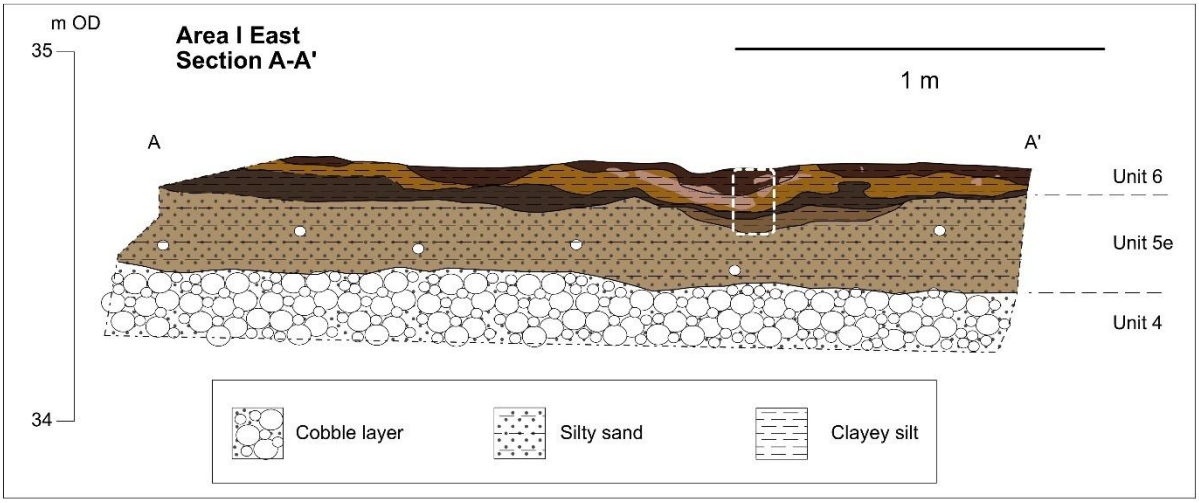

Figure 3.2. Section A-A’ following the quarry cut in Area I East. See main paper for location.

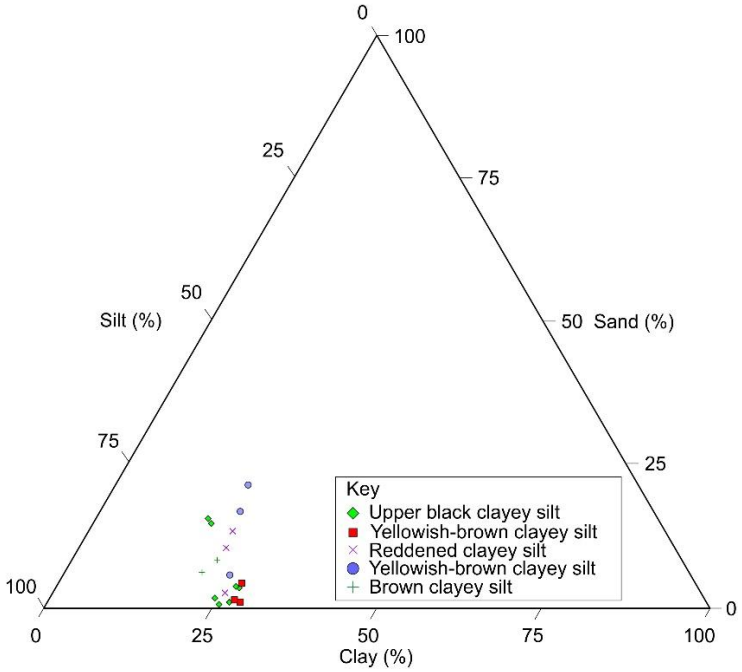

Figure 3.3. Tripartite plot of the particle size distribution of unit 6 sediments. The yellowish-brown clayey silt was sampled above and below a horizon mixed with reddened clayey silt. The column location did not provide an unmixed sample of the lower black clayey silt.

3.3. Lithological Analysis

Simon Lewis and Nick Ashton

Identification of the lithology of clasts is a widely used technique for understanding the geological source of stones in fluvial, marine or other gravel-rich deposits, which can help in understanding the processes involved in sediment formation as well as provide a means of correlation and differentiation of deposits, and reconstruction of landscape changes resulting from fluvial and glacial processes[13]. Geological work in the Breckland since 1987 has generated a large number of such studies, which provides a database of over 121,000 stone identifications from 29 sites or contexts (Tables 3.1 and 3.2). All the samples from the Barnham area were reviewed in 2024, specifically to check for presence of pyrite fragments. This database enables an independent assessment of the prevalence of pyrite in the Breckland. For these analyses, gravel samples were sieved to capture the 11.2-16.0 mm size fraction, and where clast counts are low, the 8.0-11.2 mm size fraction was also counted[12].

The Breckland encompasses three main Pleistocene sets of deposits. The first consists of pre-MIS 12 sediments of the former Bytham River sediments, which had a catchment in the English Midlands and flowed eastwards across East Anglia into the North Sea[14]. In the Breckland deposits of the Bytham are well represented and are characterised by rocks from the English Midlands, such as quartz, quartzite and carboniferous chert. The second set of deposits are the Anglian glacial sediments (tills, sands and gravels), attributed to MIS 12. The lithology is characterised by flint, sometimes chalk, and rocks from more northerly sources such as *Rhaxella* chert and Spilsby sandstone, together with smaller quantities of reworked Bytham sediments[14,15]. The Anglian glaciation destroyed the course of the Bytham river and carved out the Wash Basin. The result was that post-Anglian rivers (MIS 11 and later) flowed from central East Anglia, west and north-west into the Wash Basin. These sediments, comprising the third group, are dominated by local flint, with a smaller input from reworked Bytham fluvial and Anglian glacial sediments.

Table 3.1. Principal lithological groups given by % for Breckland sites divided by Pre-Anglian river (Bytham), Anglian glacial and post-Anglian river (Lark, Little Ouse and tributaries) deposits. Total counts for each site or context are given in final column. Numbered references are given by each site or context name.

	Quartz group[a]	Cherts[b]	Flint group	Sediment non-dur.[c]	Ign. + meta.	Others	Unident.	Pyrite	Total
Pre-Anglian (Bytham)									
Brandon Fields[14]	36.6	2.9	58.2	2.2	0.1	0.0	0.0	0.0	818
Fakenham Magna[14]	60.1	3.4	25.4	10.5	0.6	0.0	0.0	0.0	4507
Feltwell, Frimstones Pit[14]	19.5	5.3	59.5	14.5	0.1	0.0	1.1	0.0	2551
Flempton Pit[15]	35.6	7.5	53.7	2.5	0.0	0.0	0.7	0.0	1030
High Lodge (Bed C/D)[16]	56.1	7.7	29.4	5.6	0.0	0.0	1.2	0.0	337
Ingham (Bytham) [15]	71.8	9.1	16.6	1.5	0.0	0.0	1.0	0.0	2844
Lakenheath[14]	36.0	5.8	39.8	16.6	0.4	0.0	1.4	0.0	4726
Rampart Fields[14]	42.4	7.6	48.0	1.0	0.0	0.0	1.1	0.0	2224
Rushbrook[15]	56.8	9.6	31.7	0.7	0.0	0.0	1.1	0.0	271
Sapiston[14]	32.5	3.1	56.1	7.9	0.4	0.0	0.0	0.0	8395
Seven Hills[15]	79.9	6.6	12.3	0.2	0.0	0.0	0.9	0.0	423
Timworth[15]	26.7	4.3	63.0	4.6	0.0	0.0	1.4	0.0	3115
Subtotal									**31,241**
Pre-Anglian/Anglian (Bytham)									
Warren Hill[14]	31.2	5.2	51.0	12.2	0.3	0.0	0.2	0.0	19,676
Anglian									
Barnham East Farm[7]	10.4	2.1	61.7	23.2	0.2	2.2	0.1	0.0	18,935
Barnham, Kidney Plant. Pit[7]	11.8	2.8	59.9	24.5	1.0	0.0	0.0	0.0	957
Barnham, Tilbrook's Pit[7]	12.2	1.7	66.1	19.5	0.0	0.4	0.1	0.0	2499
Elveden till[17]	2.0	1.2	9.8	86.9	0.1	0.0	0.0	0.0	1538
High Lodge (Bed F-H)[16]	17.6	2.8	41.4	37.0	0.3	0.0	0.9	0.0	8226
Ingham Farm[15]	14.0	2.9	71.2	11.0	0.1	0.0	0.8	0.0	1025
Ingham[15]	5.1	2.2	59.6	32.0	0.4	0.0	0.7	0.0	1286
Weatherhill Farm Pit[18]	8.3	2.8	36.4	51.9	0.1	0.0	0.5	0.0	3768
Subtotal									**38,234**
Post Anglian (Lark/Lt. Ouse and tributaries)									
Barnham Heath[19]	8.9	1.6	84.8	4.5	0.2	0.0	0.0	0.0	10670
Broomhill Pit[19]	3.3	1.5	94.3	0.6	0.3	0.0	0.0	0.0	1588
Devereux's Pit[20]	13.5	3.4	82.5	0.5	0.1	0.0	0.0	0.0	6085
Elveden lag gravel[17]	7.4	1.9	86.9	2.3	0.5	0.0	0.9	0.0	3513
Lackford[21]	14.4	0.0	84.7	0.2	0.0	0.0	0.7	0.0	411
Redhill[19]	5.6	0.7	88.0	5.6	0.1	0.0	0.0	0.0	3932
Warren Hill (Lark)[14]	7.9	2.2	64.2	25.6	0.0	0.0	0.0	0.0	629
Warren Wood[19]	5.5	0.8	83.9	9.8	0.1	0.0	0.0	0.0	5443
Subtotal									**32,271**
TOTAL									**121,356**

a: includes quartz, quartzite, schorl, sandstone and glauconitic sandstone; b: includes Carboniferous, *Rhaxella* and other cherts; c: includes chalk, limestone, soft sandstone, ironstone and mudstone. References given by site names.

Table 3.2. Principal lithological groups given by % for Anglian (MIS 12) sediments from Barnham East Farm (BEF), Kidney Plantation Pit and Tilbrook's Pit[7], and from post Anglian sediments at Barnham Heath[19]. Total counts for each site or context are given in final column. The BEF glacial sediments directly underlie the interglacial sediments and provide the source for any coarse material within the interglacial deposits.

	Quartz group[a]	Cherts[b]	Flint group	Sediment non-dur.[c]	Ign. + meta.	Others	Unident.	Pyrite	Total
Anglian (MIS 12)									
BEF, sand and gravel	12.1	2.5	77.7	6.1	0.3	1.2	0.1	0.0	8295
BEF, till	9.5	0.9	21.0	64.0	0.0	4.6	0.0	0.0	6061
BEF, brown diamict	8.7	2.9	86.8	0.4	0.2	0.7	0.3	0.0	4579
Tilbrook's Pit	12.2	1.7	66.1	19.5	0.0	0.4	0.1	0.0	2499
Kidney Plantation Pit	11.8	2.8	59.9	24.5	1.0	0.0	0.0	0.0	957
Post-Anglian									
Barnham Heath	8.9	1.6	84.8	4.5	0.2	0.0	0.0	0.0	10,670
TOTAL									**33,061**

a: includes quartz, quartzite, schorl, sandstone and glauconitic sandstone; b: includes Carboniferous, *Rhaxella* and other cherts; c: includes chalk, limestone, soft sandstone, ironstone and mudstone.

4. Micromorphology

Sally Hoare

Micromorphological analysis at Barnham investigated potential sedimentary evidence for hearth features. Typically, they are composed of a sequence of oxidized reddened sediment overlain by a black char layer and greyish ash layer[22]. Char and ash are, however, highly susceptible to weathering and off-site erosion[23] while the cemented and reddened layer formed below a fire event is more durable. Such reddened, cemented sediment lenses where reported on Palaeolithic sites have been suggested to present evidence for fire control[24-26]. Macroscopic identification of such features is not unequivocal, however, and reddened sediment can also result from redoximorphic processes, and only microcontextual analysis can reveal their formation and integrity[27,28].

To investigate the formation of the reddened sediments and of other potential microscopic combustion related materials, seven block samples were collected for micromorphological analysis (Fig. 4.1). This included two (S1064 and S1096, Fig. 4.2) from the potentially heated sediment, and five (S1091, S1097, S1099, S1106 and S1107, Fig 4.3) from adjacent areas to enable comparison with non-heated sediments from the same units. For the block sample collected in 2022 (S1064), two thin sections (68 x 139 mm, Fig. 4.4) were produced by the Terrascope Thin Section Slides laboratory, Troyes, France. For the remaining six samples, all collected in 2023, six thin sections (76 x 110 mm) were produced by MKFactory, Stahnsdorf, Germany, of which three (S1096, S1097 and S1106) are analysed here (Figs 4.5-4.7). Analysis was conducted with Evident BX53 microscope and the cellSens software in plane- (PPL), cross-polarized (XPL) and oblique incident light (OIL) following established descriptions[29,30].

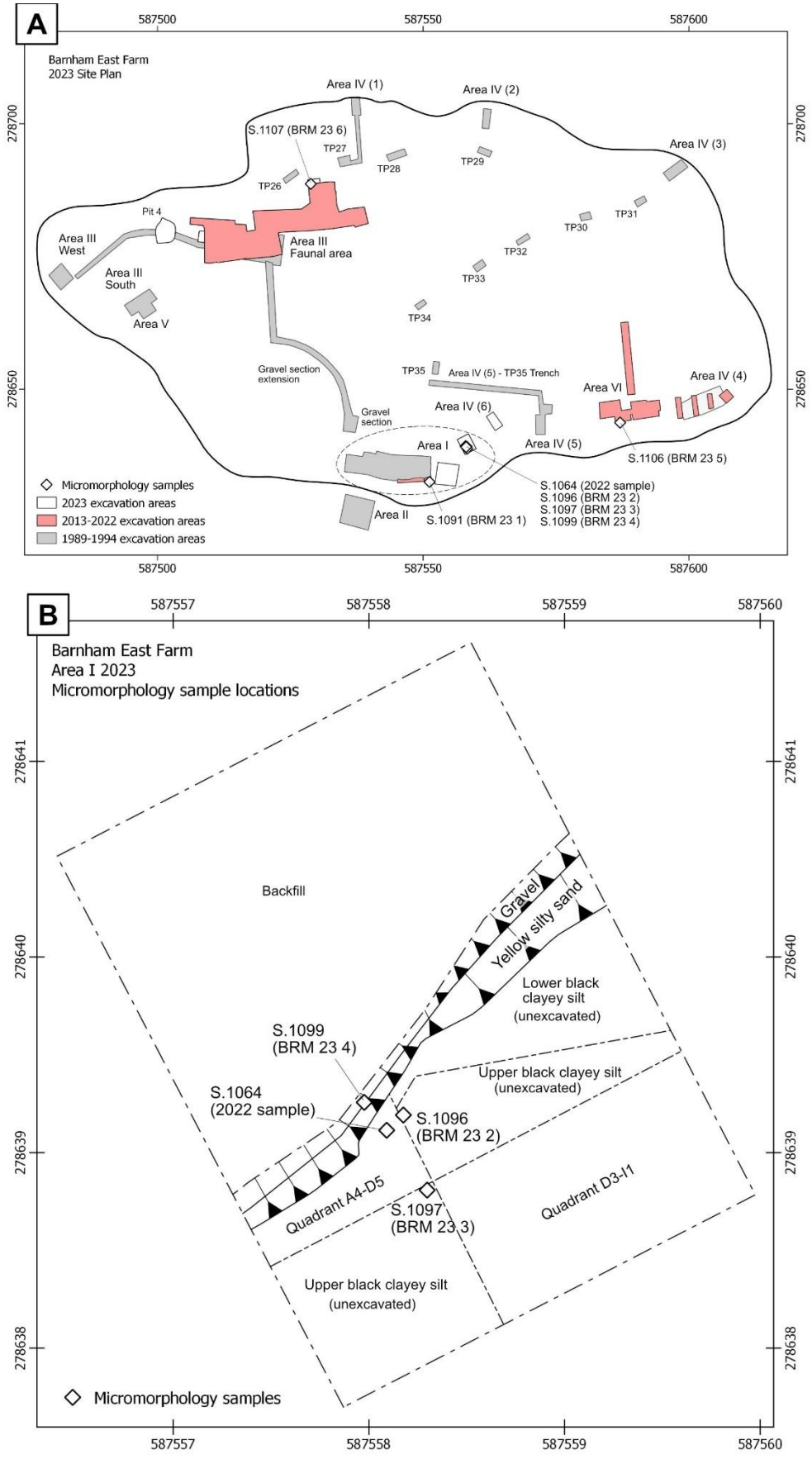

Figure 4.1. A. Site plan showing location of seven block samples collected for micromorphological analysis. **B.** 2023 post-excavation plan of Area I, showing location of block samples.

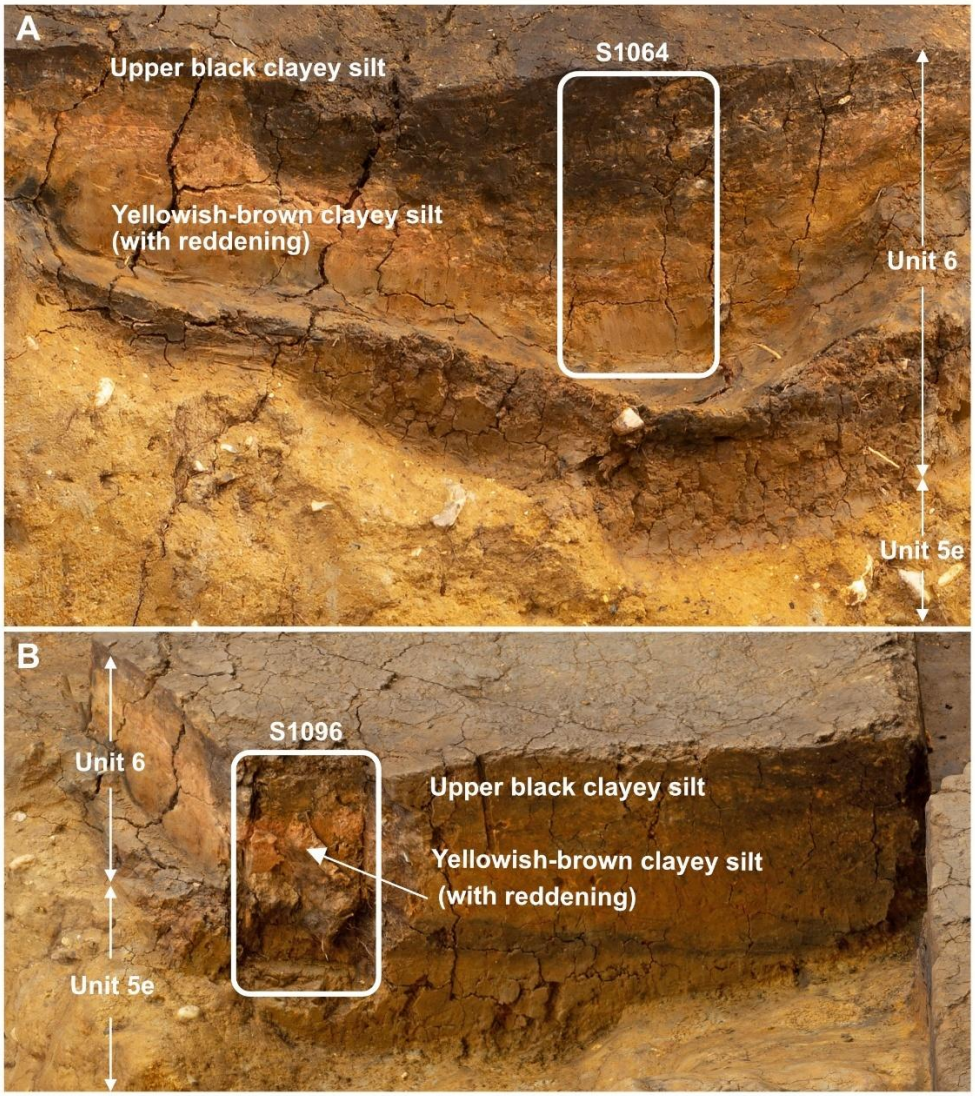

Figure 4.2 Location of block samples (**A**) S1064 (68 x 139 mm) and (**B**) S1096 (76 x 110 mm) in Area I East at the contact of the upper black clayey silt and the yellowish-brown clayey silt (with reddening). Note the clear colour difference in the yellowish-brown clayey silt with and without reddening.

The micromorphological analysis of S1064 and S1096 both confirm field observations and provide further insights into the processes occurring in the different units identified in the field as well as their temporal and spatial relationships. Both samples show the same sequence. In S1064 the yellowish-brown clayey silt (with reddening) has a dense homogenous clay matrix with silt-sized to more rarely fine or medium sand-sized quartz grains (Fig. 4.4E and F). Void space is limited to channel and chamber voids that occur throughout, but there is no aggregation, indicating low levels of bioturbation. Voids are commonly filled with clay infillings which relate to illuviation from the upper black clayey silt above (Fig. 4.4C). The clay infillings show an orange colour caused by oxidized iron. Generally, the matrix exhibits two different hues (Fig. 4.4D), either stained orange (Fig. 4.4E) similar to the clay illuviation with goethite or lepidocrocite present or reddish (Fig. 4.4F) due to haematite formation. This colour difference is most clearly expressed under oblique incident light. Haematite can form due to heating of goethite in sediments[31]. The reddish colour of the matrix is homogenous, not related to specific microfacies of the sediment and it is locally interrupted by clay illuviation from above (Fig. 4.4F), providing a temporal window.

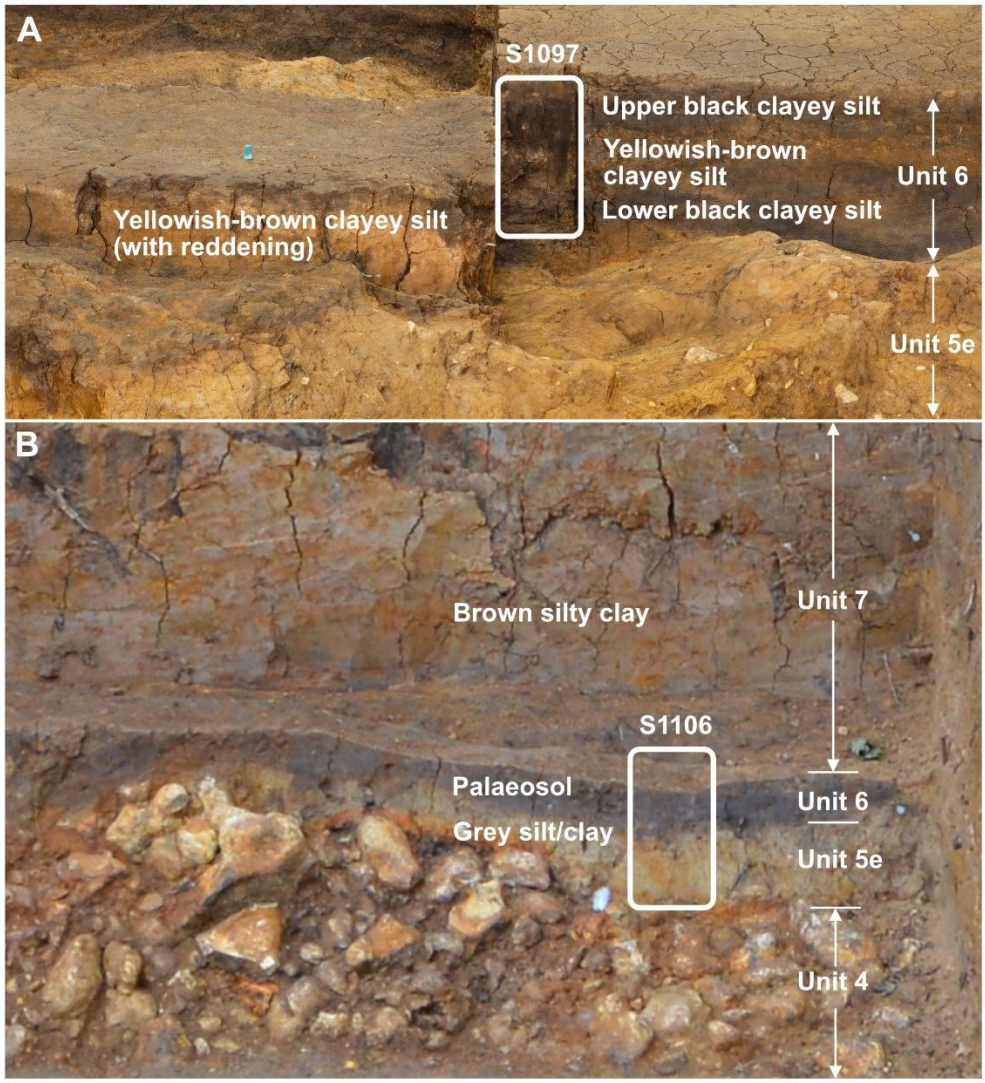

Figure 4.3 Location of block samples S1097 and S1106. **A.** S1097 is from Area I East at the contact of the upper black clayey silt and the yellowish-brown clayey silt. **B.** S1106 is located in Area VI at the contact between the palaeosol and the yellow silty sand.

Analysis of S1096 shows the same sequence, colour differences and processes as S1064 including reddening within the matrix unrelated to microfacies. The reddening is best observed under oblique incident light (Fig. 4.5B and C). The different hues are either orange caused by iron oxidation of clay illuviation or reddish caused by haematite formation. Like S1064, the reddish colour is in situ occurring within the matrix and the orange, which relates to clay infillings and coatings, within channels and voids. The clay infillings interrupt the reddening within the matrix showing the infillings to result from clay illuviation as a later process from the upper black clayey silt (Fig 4.5B). The reddish colour is homogenous throughout the sediment (Fig. 4.5C and B). No combustion related materials were observed in either thin section. The contact with the upper black clayey silt is clear in both thin sections and characterized by a colour change with a brown hue in the upper black clayey silt. This brown hue is caused by the fine distribution of amorphous organic staining (Fig. 4.4B). In one locale redeposited charred material was observed (Fig. 4.4B), indicating the presence of fire in the landscape. Also here, the same orange clay illuviation in channels and voids can be seen, but it is less developed. To summarize, the observed sequence shows soil formation with horizonation, clay infillings and illuviation, amorphous organic staining and iron oxidation. The reddening appears to be caused by haematite formation, which can be linked to heating, and the feature is in situ.

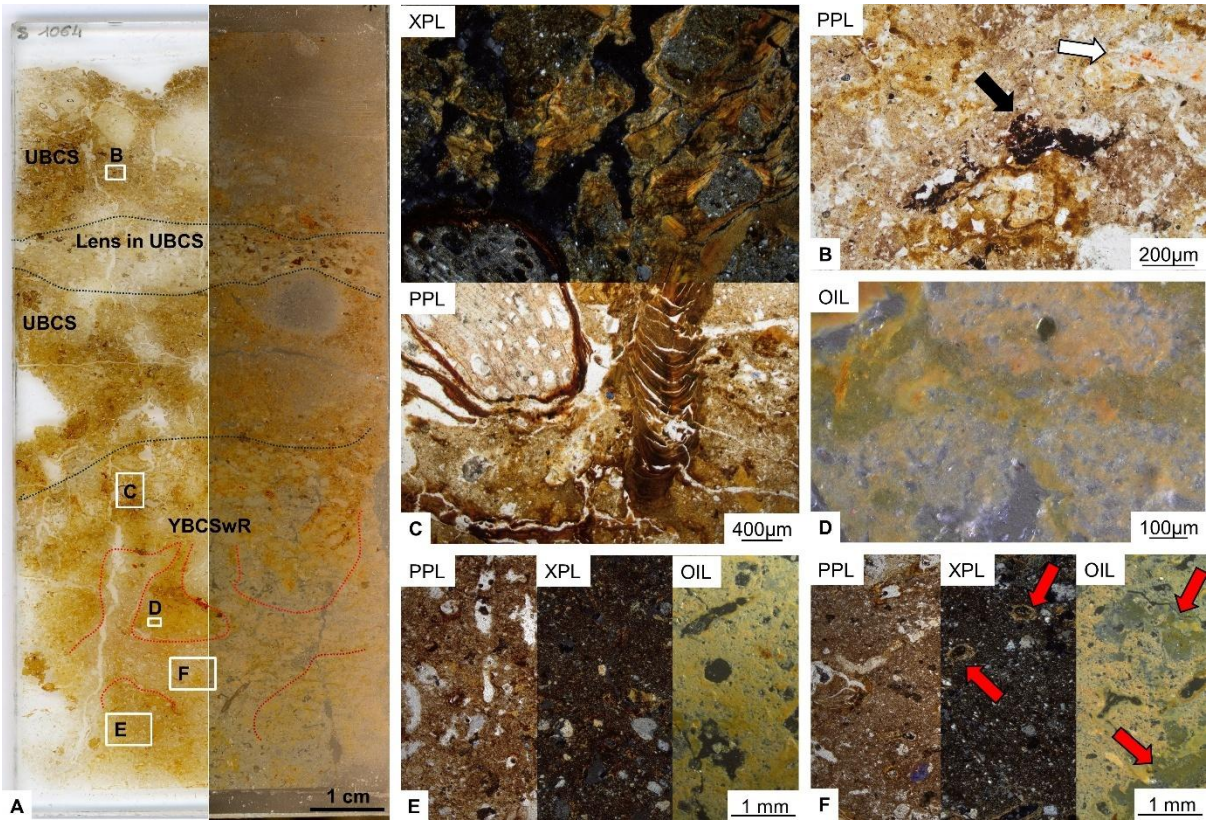

Figure 4.4. Micromorphological analysis of sample S1064 (68 x 139 mm) with upper black clayey silt (UBCS), interpreted as a palaeosol, and the yellowish-brown clayey silt with reddening (YBCSwR). **A.** Scan of thin section S1064 with open (left) closed (right) scanner lid. The sedimentary sequence contained within this thin section encompasses the YBCSwR overlain with a clear contact by the UBCS. The UBCS contains a lens of light brown material here that appears similar to the YBCS. Note that the matrix in the YBCS exhibits two different shades of staining, orange and reddish (indicated by a red line). White boxes indicate the location of microphotographs B-F. **B.** Microphotograph from the UBCS showing a silty clay groundmass, similar to the YBCS, but with dark brown humic and orange iron staining. Iron staining is mainly related to voids occurring as coatings around clay infillings. Note also the occurrence of charred plant residue (black arrow), which appears redeposited and indicates a landscape fire, and a piece of flint (white arrow). **C.** Microphotograph at the top of the YBCS (in XPL and PPL) exhibiting well developed and iron stained clay infillings indicating soil formation related to the UBCS. The nearly radial section of a root provides further evidence of plant growth, but this may be a recent feature. **D.** Microphotograph of the YBCS exhibiting orange staining of clay infillings and a generally reddish staining of the matrix indicating that both formed in situ and that the orange staining is a comparably more recent feature related to clay translocation down through the profile, filling voids and iron oxidation. **E.** Microphotograph of the orange stained YBCS with different light sources. The groundmass is composed of brownish clay (in XPL and PPL) with silt sized quartz grains, very rarely sand sized, and in an open porphyric related distribution. In XPL and OIL iron stained, orange clay infillings in voids is apparent whereas in OIL homogenous orange staining of the matrix is also observable. **F.** Microphotograph of the reddish stained YBCS with different light sources. The groundmass is composed of brownish clay (PPL and XPL) with silty sized quartz grains, very rarely sand sized, with an open porphyric related distribution. A few channels are apparent and dark brown amorphous staining. In XPL, occasional clay infilling is visible (red arrow), but less common than in the orange stained YBCS (Fig. E). The starkest contrast to the orange stained YBCS becomes apparent in OIL, the matrix here exhibits a reddish hue. Note that in areas of clay infillings (red arrow) the colour remains orange to brownish.

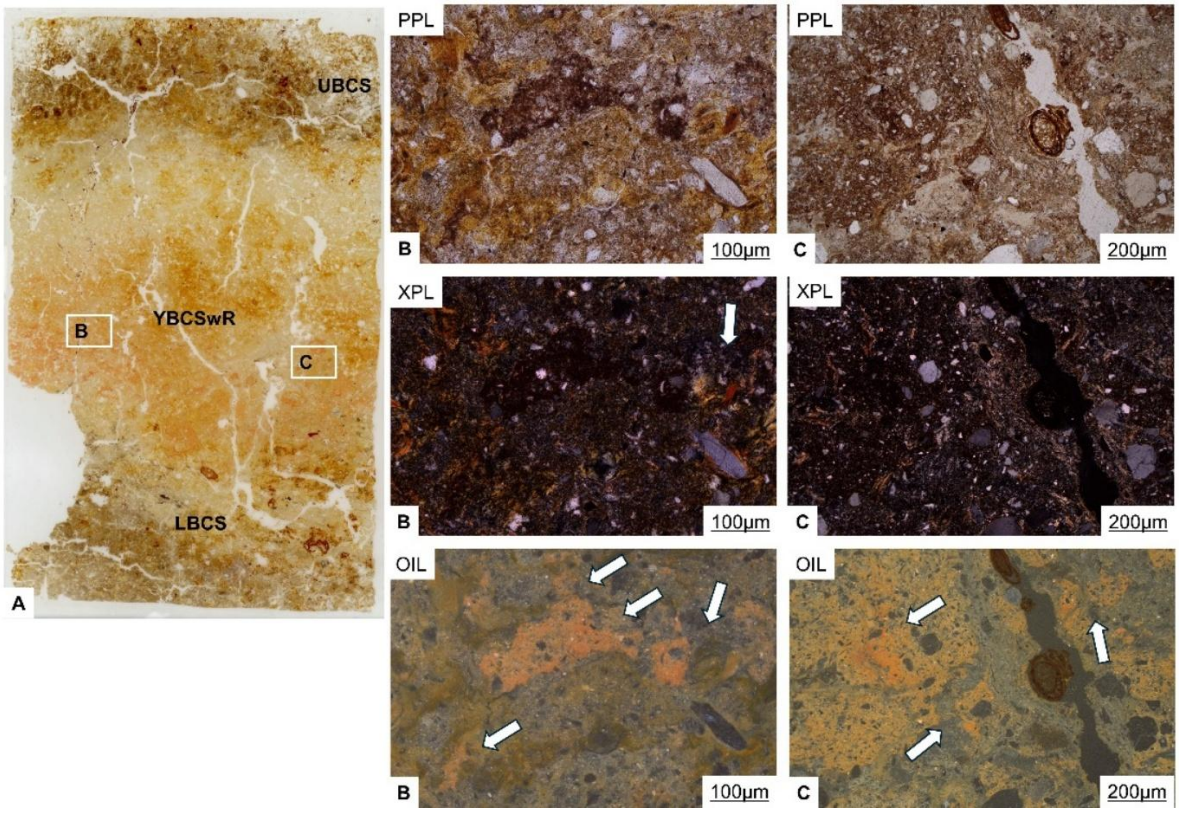

Figure 4.5 Micromorphological analysis of sample S1096 yellowish-brown clayey silt with reddening (YBCSwR), and upper black clayey silt (UBCS) and lower black clayey silt (LBCS), interpreted as upper and lower palaeosols. **A**. Scan of thin section S1096 (76 x110 mm) with open scanner lid. The sedimentary sequence contained within the thin section encompasses the YBCS with reddening which is underlain and overlain with the LBCS and UBCS. The matrix exhibits different hues, orange or red. White boxes indicate the location of the microphotographs B and C. **B.** Microphotographs from the YBCS using different light sources showing the reddening as homogenous within the matrix and unrelated to clay infillings in PPL, XPL and OIL. The reddening is also interrupted by clay infillings which occur as a later process providing a temporal window (shown by white arrows) **C.** Microphotographs (PPL, XPL and OIL) from the YBCS showing the different hues. The reddening is homogenous within the matrix and unrelated to clay infillings. Sections of roots are also present within a channel providing evidence of plant growth. However, these may be recent features.

The micromorphological analyses of samples S1097 and S1106 were undertaken to provide further comparison of the same sedimentary units from other areas of the site potentially not subject to heat alteration (Fig. 4.1). In S1097, the yellowish-brown clayey silt has a dense homogenous clay matrix with silt-sized to more rarely fine or medium sand-sized quartz grains. Void space occurs as mainly channel and chamber voids (Fig. 4.6B). Void spaces are commonly filled with clay infillings related to the palaeosol above (Fig. 4.6C). The clay infillings show different hues either orange or brown relating to iron oxidation with some possible reddening occurring within void spaces (Fig. 4.6C). Iron nodules are also present, *in situ*, and some exhibit a reddish hue indicating haematite formation (Fig. 4.6D). The matrix of the yellowish-brown clayey silt shows no reddening in the sample (Figs 4.6B and C). Reddening in this thin section only relates to formation of natural features such as iron nodules on the overlying palaeosol (Figs 4.6C and D). The contact with the overlying palaeosol is clear and characterised by a colour change with a brown hue in the palaeosol. Evidence of fire is also present within the upper palaeosol in the form of in situ charred root remains within a channel which could represent a landscape fire (Fig 4.6F) and the presence of reddened aggregates which could either be reworked from the heated sediments below (e.g. S1096) or indicate a second fire event of yet unknown origin (Fig 4.6G). To summarize, the observed sequence is like that of

S1064 and S1096 showing soil formation with horizonation, clay illuviation, amorphous organic staining and iron oxidation but without reddening of the matrix in the yellowish-brown clayey silt demonstrating the heated sediment in S1096 and S1064 to be a localized and restricted feature.

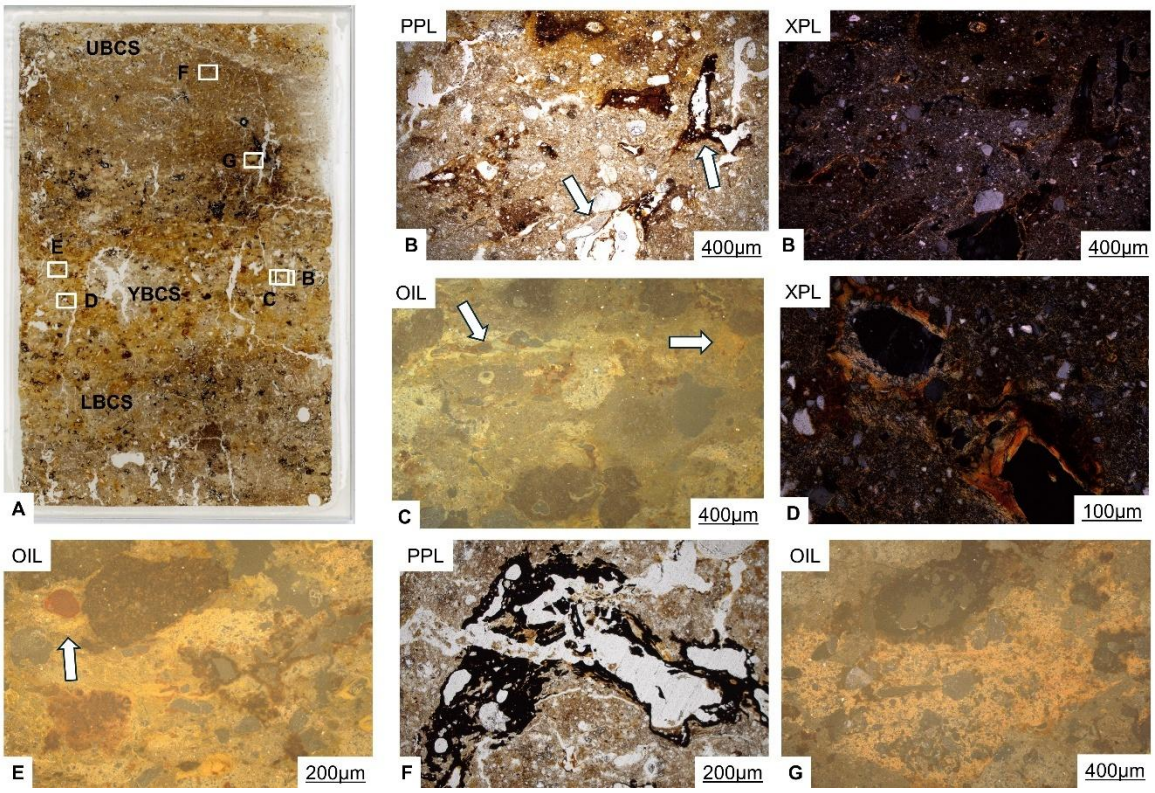

Figure 4.6 Micromorphological analysis of samples S1097 upper black clayey silt (UBCS) interpreted as a palaeosol and the yellowish-brown clayey silt without reddening (YBCS). **A.** Scan of thin section S1097 (76 x 110 mm) with open scanner lid. The sedimentary sequence contained within the thin section encompasses the yellowish-brown clayey silt without reddening which is underlain and overlain by the LBCS and UBCS. White boxes indicate the location of the microphotographs B-G. **B.** Microphotograph from the YBCS showing matrix, void spaces and clay infillings attributed to clay illuviation in PPL and XPL. White arrows mark the presence of the remains of plant material within some of the void spaces. The matrix exhibits different hues brown and orange. The orange relates to iron oxidation staining **C.** Microphotograph of the groundmass in OIL. The matrix varies between brown and orange but shows no evidence of reddening in the YBCS. There is some dark brown and orange iron staining of clay coatings around void spaces marked by white arrows in OIL. **D**. Microphotograph of the YBCS showing clay infillings around a void space in OIL. The clay infilling exhibits orange and brown staining relating to clay translocation within the void spaces and iron oxidation (also C). **E.** Microphotograph of a reddened iron haematite nodule marked by white arrow. The nodule forms by an accumulation of oxidized iron in the matrix and is unrelated to heating. **F.** Microphotograph in PPL of the UBCS showing the remains of charred plant tissue within a void, interpreted as a possible charred root which could indicate the presence of landscape fires. **G**. Microphotograph in OIL of a reddened aggregate in the UBCS which could be reworked from the underlying adjacent heated sediments or from a later fire event.

Micromorphological analysis of S1106 was undertaken to investigate possible heat alteration of sediments from Area VI. In this location, the palaeosol lies on a grey silt/clay, which is a lateral equivalent of the yellow silty sand in Area I (unit 5e), and is overlain by brown silty clay (unit 7). In S1106, the palaeosol has a dense silty clay homogenous groundmass with mainly silt sized quartz grains (Fig. 4.7B). Void spaces occur as channel and chamber voids the frequency of which increase towards the top of the sample (Fig. 4.7A and C). The matrix exhibits an orange and dark brown hue

which can be attributed to iron oxidation staining of clay infillings within void spaces and dark brown humic organic staining (Fig. 4.7B, C and E). Some of the channels preserve roots and organic material which could be later features (Fig. 4.7F). The top of the thin section shows a distinct colour contrast to a lighter brown hue and evidence for horizonation (Fig. 4.7A and D). The lighter hue is due to an increase in void spaces and infilling with clay which varies in colour from mainly brown and orange to reddening. The reddening is limited to void spaces and relates only to iron oxidation of clay infillings and not heating (Fig. 4.7D). Some roots are present in void spaces but are not well preserved (Fig. 4.7F). In summary, the observed sequence shows soil formation with horizonation, clay infillings related to illuviation, organic staining and iron oxidation of the clay. There is no reddening observed with the matrix or groundmass further confirming the heated sediment in S1096 and S1064 to be a localized feature.

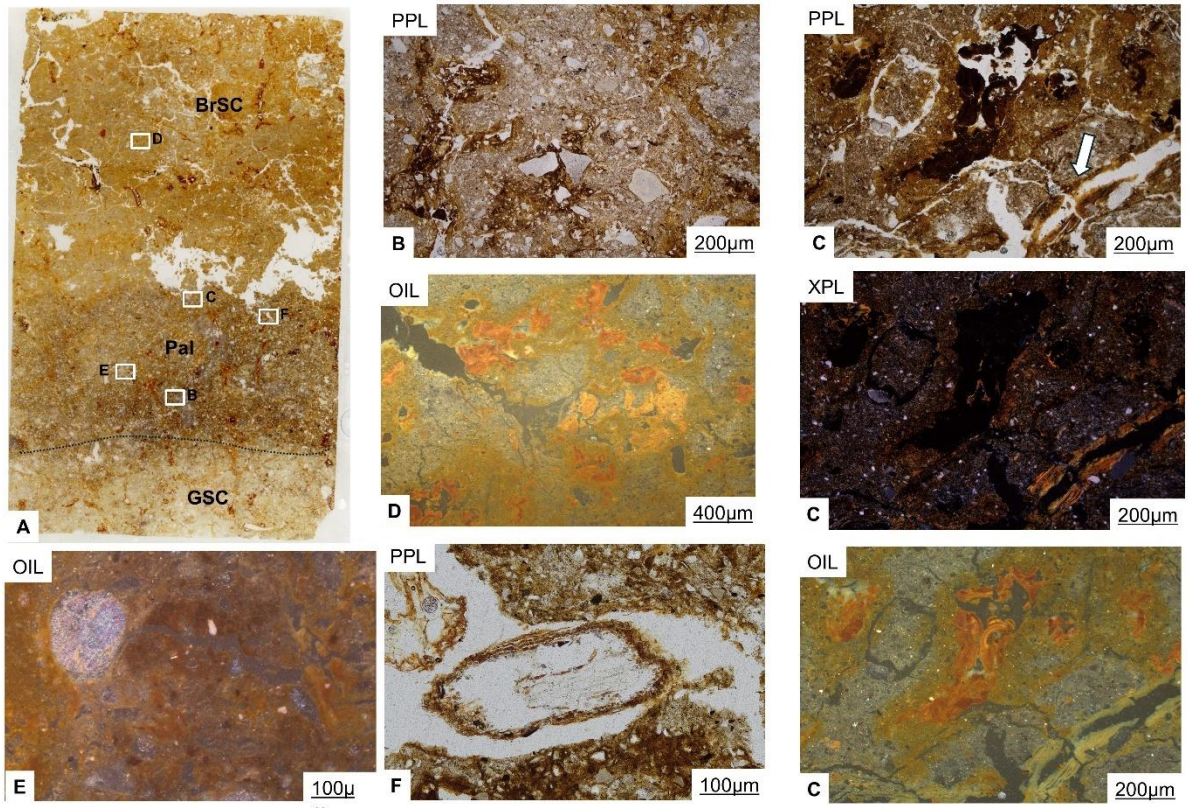

Figure 4.7 Micromorphological analysis of sample S1106 unit 6, interpreted as a palaeosol (pal), the underlying grey silty clay (GSC), which is Unit 5e in Area I West, and the overlying brown silty clay (BrSC) of unit 7. **A.** Scan of thin sections S1106 (76 x 110 mm) with open scanner lid. The sedimentary sequence contained within the thin section encompasses the palaeosol without reddening which is underlain by unit 5e and overlain by unit 7. The dark brown matrix of the palaeosol contrasts with the more orange hue of unit 7 (top). White boxes indicate the location of the microphotographs B-F. **B.** Microphotograph from the palaeosol showing the groundmass and grain size distribution including quartz grains. **C.** Microphotograph showing iron staining of clay infillings around void spaces containing roots in PPL, XPL and OIL. Note that the colour of the clay infillings and coatings varies between light brown, orange and red which is best seen in OIL. The reddening occurs only within void spaces and is not related to the matrix. Some of the channels contain roots marked by a white arrow in PPL. **D.** Microphotograph of the groundmass of unit 7 showing the lighter brown hue within the matrix and orange and red staining of clay infillings due to iron oxidation around voids. **E.** Microphotograph of the groundmass in OIL the darker brown hue due to iron oxidation and staining of amorphous organic material. **F.** Microphotograph in PPL of a root within a channel from the top of the palaeosol providing evidence of plant growth. As roots are not well-preserved within this thin section this may be a more recent feature.

5. Environmental magnetism and heating

Sally Hoare

Environmental magnetism uses mineral magnetic parameters as proxies for examining the neoformation, alteration and transportation of magnetic minerals in a variety of sedimentary archives to investigate issues such as climate and palaeoenvironment change[32], sediment source tracing[33] and fire history[34]. The application of environmental magnetism to archaeological problems has become more frequent over the last two decades including investigations of taphonomic processes and environmental modelling and the study of prehistoric combustion features or hearths[27,35-40]. The discipline has a long history of investigating the formation and response of mineral magnetic assemblages under various heating conditions[41,42]. Numerous investigations have demonstrated that magnetic enhancement in the surface sediments of combustion features (both anthropogenic and those produced by natural fires) is due to the pyrogenic formation of fine to ultrafine ferrimagnetic minerals or SFMs[33,37]. These SFMs are magnetically strong which can cause an increase in magnetic susceptibility (MS) and frequency-dependency of magnetic susceptibility (χ_{FD})[43]. SFMs are formed by a variety of environmental processes which include heating, pedogenesis, magnetotactic bacteria and volcanic activity. It is however possible to determine the source of their origin, whether heating or pedogenesis, in soils and sediments using standard approaches[37,44]. Magnetic susceptibility values can also increase due to the neoformation or increased concentrations of magnetite and or/maghemite. Reductions in MS values can also occur during heating due to the inversion of magnetite/maghemite to the magnetically weaker mineral haematite at both higher temperatures or under conditions of heating longevity[45]. Both environmental and rock magnetic methods have been employed to investigate the nature of heating processes in anthropogenic combustion features at Palaeolithic sites[27,39,46,47].

5.1. Environmental magnetic methods

All types of rocks and sediments contain varied quantities and types of magnetic minerals, the most common being the iron oxides. By characterising the response of sediment samples to laboratory applied magnetic fields, estimations can be made of the composition, concentration and magnetic domain or grain size distribution of magnetic minerals especially the iron oxides, which include magnetite (Fe_3O_4), maghemite (γFe_2O_3) and haematite (αFe_2O_3)[33]. This information can then be used to reconstruct past heating conditions as the nature of the soil or sediment magnetic iron oxide assemblages is often closely linked with external factors, including temperature, source, frequency and longevity of heating[28,36,37,39,45,48-50].

Sediments samples were pre-packed into 10 cc diamagnetic (plastic) pots and then subjected to the following sequence of standard magnetic measurements[51]. Low frequency magnetic susceptibility (χ_{LF}) was measured at 0.47 kHz and high frequency magnetic susceptibility (χ_{HF}) at 4.7 kHz, using a Bartingdon MS2 meter to assess bulk magnetic mineral concentrations. The difference between the two measurements gives the frequency dependent susceptibility expressed as either mass specific property (χ_{FD}) or as a percentage of χ_{LF}, χ_{FD}%. The loss of susceptibility between χ_{LF} and χ_{HF} reflects the response of grains that lie at the border between Single Domain (SD) and superparamagnetic (SP) grains[52]. Values of χ_{FD} provide an indication of the concentration of fine grains (ferrimagnetic magnetite/maghemite) which form during weathering and pedogenesis and heating[53]. Anhysteretic Remanent Magnetisation (ARM) was imparted using a DTECH alternating field demagnetizer with a peak alternating field of 100 mT and a direct current (DC) biasing field of 0.1 mT. Plotted values have been normalised for the DC biasing field and expressed as χ_{ARM}. Saturation Isothermal Remanent Magnetisation (SIRM) using a 1 T field generated by an MMPM5 Pulse Magnetiser. Reverse field

demagnetisation at fields of -20 mT, -40 mT, -100 mT and -300 mT was then performed and samples were directly exposed to IRM reverse immediately after SIRM. All remanence measurements were made using a Molspin fluxgate spinner magnetometer with a noise level of 0.1 x 10^{-8} A m. Results are described following previous studies[32,37,43,48].

Table 5.1. Magnetic parameters and interparametric ratios used in this part of the study, their units and interpretation.

Magnetic parameters & ratios	Units	Interpretation
Low frequency magnetic susceptibility (χ_{LF}) or Magnetic susceptibility (MS)	10^{-8} m^3/kg	Sensitive to bulk ferrimagnetic mineral content & also superparamagnetic and coarse multi-domain grains
Frequency-dependent magnetic susceptibility (χ_{FD})	10^{-8} m^3/kg	Indicates concentration of superparamagnetic ferrimagnetic grains (SP grains form via heating or pedogenesis)
Frequency-dependent magnetic susceptibility (χ_{FD} %)	%	Indicates the proportional contribution of SP grain to the bulk MS measurement
Anhysteretic remanent magnetisation (χ_{ARM})	10^{-8} m^3/kg	Sensitive to the concentration of ferrimagnetic grains in the single domain range
SIRM	$10^{-5}Am^2kg^{-1}$	Sensitive to the concentration of remanence holding material (ferromagnetic)
S ratio (-300Mt)	-	Sensitive to the concentration of antiferromagnetic minerals
χ_{ARM} /SIRM	10^{-3}/Am	Sensitive to ferrimagnetic grain size in the SD range. Ratio is known to increase with intensity of pedogenesis and heating
χ_{ARM}/χ_{LF} versus χ_{ARM}/χ_{FD}	-	Indicates whether SFMs were formed via (pyrogenic (heated), pedogenic (soil forming) processes or due to the presence of magnetotatic bacteria

5.2. Barnham samples

The magnetic properties of five sediment samples were analysed using environmental magnetic methods from the possible combustion feature. Samples 1053, 1054 and 1100 were taken directly from the reddened clayey silt (purported heat altered sediment) and samples 1056 and 1055 from the adjacent unaltered substrate, the yellowish-brown clayey silt. A large sample was also taken of this sediment to create an experimental reference data set to evaluate the impact of different heating processes on the magnetic properties.

5.3. Experimental design

The experimental design followed previous archaeomagnetic fire studies[27,28,36,37,39,45,54] to investigate: 1. whether the magnetic properties of the reddened clayey silt arose from heating or natural processes (pedogenesis) and if from heating; 2. did they result from relighting events (human action) or single, longer heating events (natural fire or human action). Due to the large number of experiments required for this study and limited availability of archaeological substrate, we were only able to conduct laboratory-based experiments. Four experiments (1-4) were conducted to characterise changes in the magnetic properties of the yellowish-brown clayey silt when exposed to single extensive heating events of different durations and to successive episodes of heating at different temperature ranges.

1. Step wise incremental heating experiment of the unaltered substrate. Heating for four hours in a muffle furnace at temperature increments of 100 °C from 100 to 1000 °C.
2. Step wise incremental reheating experiments of the unaltered substrate for (4, 12, 24 and 48 hours) and at different temperature ranges (300, 400, 500, 600, 700 and 900 °C). Each experiment was then repeated successively (4 repeats for the 4- and 12-hour

heating times and 2 repeats for the 24- and 48-hour heating times. The lower number for the longer heating times was due to inversion to haematite on the second experiment which is not representative of the mineralogy of the archaeological samples).

3. Experiments to calculate χmax.
4. Additional heating experiments x 12 and 24 times for 4 and 12 hours (400 and 600 °C).

The mineral magnetic parameters of MS and χ_{FD}% were applied to all experiments. The magnetic mineralogy and magnetic grain size were further examined using ARM and SIRM and backfield measurements for each experiment on the first and then either the second or fourth episode of heating only, depending on the results. This is because the application of magnetic fields to determine χ_{ARM}/SIRM and S-ratio values alters the magnetic properties of the sample. It is possible to demagnetize the sample which returns its properties back to its original state. However, as some of the changes were so small between the heating episodes (e.g., MS = 1-3 x 10^{-8} m^3/kg^{-1}), changes between the first and subsequent heating episodes may not have been detectable in terms of potential losses in MS due to demagnetisation effects. In this regard small losses could have affected the results and interpretation.

5.4. Experiment 1 stepwise incremental heating experiment

Experiment 1 captured the response of the magnetic properties of the unaltered substrate to heating at 100 °C temperature increments from 0 to 1000 °C (Fig. 5.1) showing how changes in magnetic properties with increasing temperatures can be divided into four phases. The magnetic properties of phase 1 (unheated control sample) have a very low MS value (8.57 x 10^{-8} m^3/kg^{-1}). The S-ratio indicates that the mineralogy is magnetite with significant contribution from haematite (as much as 50%). The magnetic grain size is coarse single domain with a low percentage of SP grains. Little difference is observed in the magnetic properties of the samples heated to 100 and 200 °C. As the temperature increases during phase 2, to 300 to 400 °C, there is an increase in MS values, χ_{FD}% and $\chi_{ARM,}$ along with SIRM and higher S-ratio values. Values in all parameters continue to increase up to 700 °C. These increases are due to the neoformation of magnetically strong minerals, specifically fine to ultrafine stable single domain (SSD) and superparamagnetic (SP) magnetite/maghemite grains along with a higher concentration of magnetite/maghemite. Peak values are observed in MS and χ_{FD}% at 600 °C and in the parameters of χ_{ARM} and SIRM at 700 °C. At these temperatures, there is also an increase in the concentration of magnetite and or maghemite indicated by higher S-ratio and SIRM values. During phase 3, and between temperatures of 700 and 800 °C, the destruction of ferrimagnetic minerals (decrease in all parameters) results in the complete inversion of magnetite/maghemite to haematite as the final phase 4 at 900 °C.

5.5. Magnetic properties of the Barnham archaeological samples

The magnetic properties of the reddened clayey silt (1054, 1053 and 1100) and yellowish-brown clayey silt (1056, 1055) are listed in Table 5.2. The reddened clayey silt samples contain large quantities of secondary fine grained ferrimagnetic minerals, SFMs, (high χ_{ARM} and χ_{FD}% values), which can form through a variety of environmental processes including heating, pedogenesis and magnetotactic bacteria. To determine their origin, the ratios of χ_{ARM}/χ_{LF} versus χ_{ARM}/χ_{FD} were used which measure the magnetic grain size distribution and can differentiate between the origins of SFMs in soil/sediment samples whether pyrogenic or pedogenic[47]. The reddened clayey silt samples yielded specific ratios of χ_{ARM}/χ_{LF} versus χ_{ARM}/χ_{FD} (3.44 vs 36.35, 3.19 vs 30.18 and 3 vs 34.6) respectively, which places them firmly within the range of values for pyrogenic origin only. The magnetic mineralogy is dominated by magnetite with little contribution from haematite (1100) and magnetite with some contribution from haematite (1053, 1054) and they contain high

concentrations of SP minerals (χ_{FD}% values of 9.4 to 11.1). All three samples contain quantities of coarse single domain grains having χ_{ARM}/SIRM values of 0.50, 0.51 and 0.57.

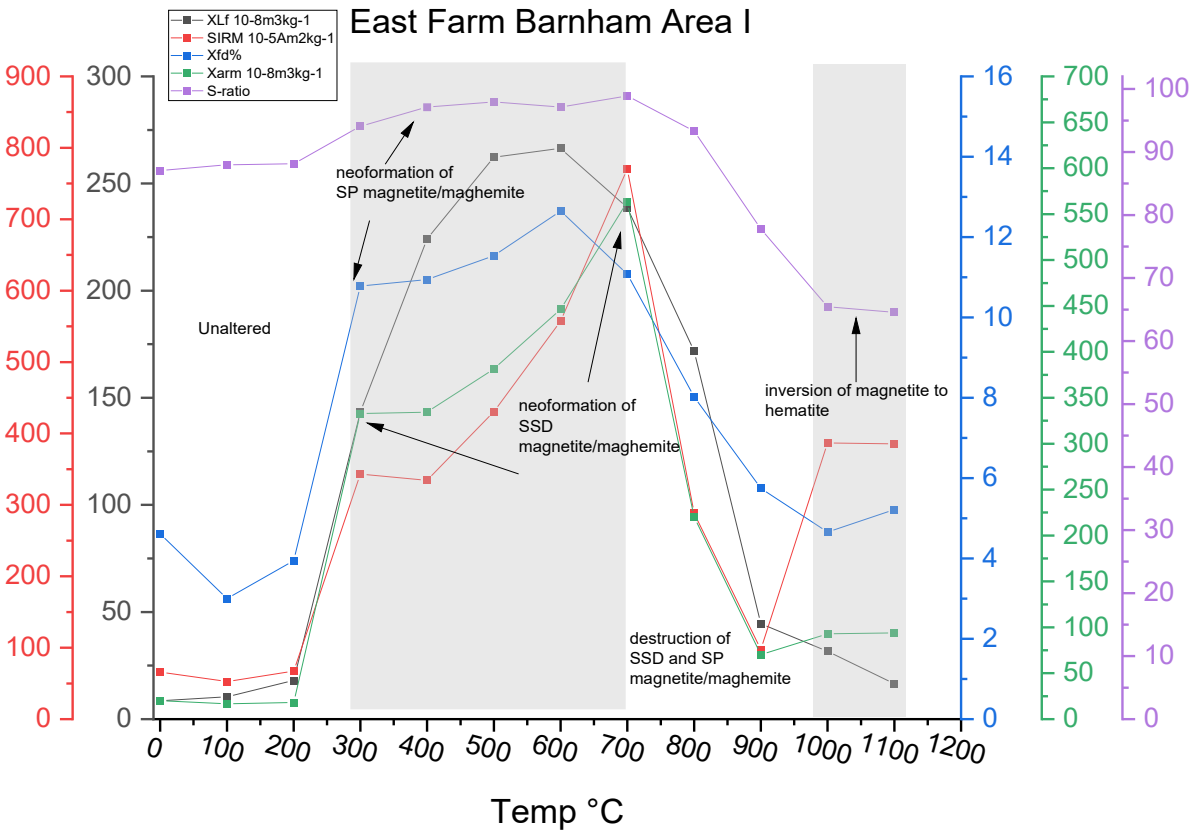

Figure 5.1. Results of experiment 1 (incremental heating experiment) for the yellowish-brown clayey silt. The x-axis shows the temperature in degrees Celsius (C) ranging from 0 to 1100 in 100 degree C increments. The y-axis shows the magnetic parameters used in the experiments. Displayed on the right the type of magnetic mineral (S-ratio) and magnetic grain sizes $\chi_{ARM/}$ and χ_{FD}% on the left the magnetic susceptibility or (χ_{LF}) and concentration dependent parameter SIRM. This set of experiments was conducted once.

Table 5.2. The magnetic properties of samples taken from the reddened clayey silt (RCS: 1054, 1053 and 1100) and yellowish-brown clayey silt (YBCS: 1056 and 1055). The final column marks the samples in which the origin of the magnetic properties was determined to have resulted from pyrogenic (pyr) or pedogenic (ped) processes. These origins were determined following a previous approach[37], which provides defined values for each process using the ratios of χ_{ARM}/χ_{LF} versus χ_{ARM}/χ_{FD} (samples marked with an x did not meet the minimum criteria set out by the authors for this approach).

Sample Nos	MS (χ_{LF} 10^{-8} m^3kg^{-1})	χ_{FD} 10^{-8} m^3kg^{-1}	χ_{FD}%	χ_{ARM} 10^{-8} m^3kg^{-1}	SIRM 10^{-5} Am^2kg^{-1}	S-ratio	χ_{ARM}/SIRM $10^{-3}mA^{-1}$	χ_{ARM}/χ_{FD}	χ_{ARM}/χ_{LF}	Pyr/Ped origin
1056 (YBCS)	8.57	0.39	4.61	20.23	65.90	87.05	0.306	51.09	2.35	X
1055 (YBCS)	8.01	0.36	4.59	21.66	63.44	87.14	0.34	58.76	2.7	X
1054 (RCS)	14.97	1.41	9.46	51.54	100.48	92.06	0.51	36.35	3.44	Pyr
1053 (RCS)	17.76	1.88	10.58	56.78	112	92.26	0.50	30.18	3.19	Pyr
1100 (RCS)	19	1.67	11.19	58.12	100.24	95.01	0.57	34.60	3.05	Pyr

From experiment 1, the magnetic properties of the reddened clayey silt samples have higher quantities of pyrogenically formed SFMs and double the MS and ARM values compared to the unaltered substrate of yellowish-brown clayey silt. The reddened clayey silt samples also differ from the incremental heating experiment as they have significantly lower MS and χ_{ARM}/SIRM values than the samples in phases 2 and 3. Furthermore, the samples exposed to higher temperatures above 800 °C, or phase 4, are characterized by much higher concentrations of haematite (lower S-ratio values) and lower χ_{FD}% values. This suggests that the magnetic properties of the reddened clayey silt could have arisen from a different heating process from experiment 1 (e.g., more than one episode of heating or a single more extensive heating events) or, that they may have been subject to taphonomic alteration or contain material of variable origins.

5.6. Experiment 2

A further experiment was conducted to investigate whether the low MS and χ_{ARM}/SIRM values of the reddened clayey silt could have resulted from a different heating process to experiment 1, specifically whether the magnetic properties could have arisen from either successive relighting events or single more extensive heating events of different durations and temperatures. The results (Table 5.3) are summarised by the MS (χ_{LF} x 10^{-8} m^3/kg^{-1}), χ_{FD}%, S-ratio and χ_{ARM}/SIRM values.

4-hour successive heating experiment. The MS values (Table 5.3) are highest relative to the unheated control samples on the first episode of heating at temperatures of 500 and 600 °C than at 300, 400 and 700 °C. At temperatures of 900 °C, MS values are the lowest in the data set, but are still four times higher than the unheated control sample. At temperatures of 300 to 700 °C and with each successive episode of heating, we see further magnetic enhancement and higher MS and χ_{FD}% values. The largest increase in MS values is observed on the first two episodes of heating, regardless of temperature, whereas increases on the 3rd and 4th episodes are much smaller and averaged between (1-3 x 10^{-8} m^3/kg^{-1}). At temperatures of 900 °C, both MS and χ_{FD}% values reduce with each successive episode of heating.

12-, 24- and 48-hour successive heating experiments. As the samples are exposed to heat for longer periods, in 12-hour increments, the degree of magnetic enhancement and MS values are higher on the first episode at 12 hours but lower at both 24 and 48 hours. At 12 hours, increases in both MS and χ_{FD}% values with each successive episode of heating are higher than the 4-hour experiment (e.g. when heated for 4 hours at 600 °C, MS values increase from 266 to 274 x 10^{-8} m^3/kg^{-1}, and from 294 to 315 x 10^{-8} m^3/kg^{-1} when heated for 12 hours at the same temperature). However, at 24 and 48 hours, we see a major difference, when both the MS and χ_{FD}% values increase on episode 1 and reduce substantially on episode 2. These results also vary according to temperature and are more pronounced between 500 and 700 °C. For example, MS values increase on the first episode of heating for 24 hours to 214 x 10^{-8} m^3/kg^{-1} but reduce to 25 x 10^{-8} m^3/kg^{-1} on the second. When heated for 48 hours at the same temperature, the MS values are 32 x 10^{-8} m^3/kg^{-1} on the first episode of heating and reduce to 9 x 10^{-8} m^3/kg^{-1} on the second. Frequency dependency of MS values also reduces on the second episode of heating for both the 24 and 48 experiments.

S-ratio and χ_{ARM}/SIRM values – experiments 1 and 2. The magnetic mineralogy and magnetic grain sizes (SSD) were determined using the S-ratio and the ratio of χ_{ARM}/SIRM on the first and then, either the second or fourth episode of heating depending on the results. The results for the 4 and 12 hour experiments were similar. The S-ratio values for each experiment in the 300 to 700 °C temperature range, were between 92.4 and 98.9% which is characteristic of magnetic mineralogy dominated by magnetite/maghemite, the concentration of which is lower on the fourth episode. For example, heating at 600 °C for 4 hours results in a decrease in the S-ratio from 97.4 to 95.7%. Changes in the

magnetic grain size follow a similar trajectory and are also lower on the fourth than the first episode of heating. The ratio of χ_{ARM}/SIRM ranges between 0.71 and 0.99 and is characteristic of coarse to fine stable single domain grains. The coarse SSD grains are formed only in samples heated at 700 °C. At higher temperatures of 900 °C, the S-ratio values are the lowest being 77–69%, indicating mineralogy dominated by haematite, the concentration of which increases between the first and fourth episode of heating. The magnetic grain size is coarse single domain for all samples. The ratio of χ_{ARM}/SIRM also decreases between the first and fourth episode of heating at this temperature range.

As heat exposure is increased up to 24 and 48 hours, the response recorded in the magnetic properties changes substantially. At temperatures of 300 and 400 °C, the S-ratio values are higher than the unheated control sample (91 and 89) but much lower than those of the 4 and 12 hour experiments (97 and 96) on the first episode of heating. On the second episode of heating at both 24 and 48 hours, the S-ratio values reduce (to 90 and 88). The range of χ_{ARM}/SIRM ratios (0.89 to 0.81) indicates dominance of fine SSD grains, which reduce on the second episode of heating.

As the temperature is increased for the 24 and 48 hour heating times to between 500 and 700 °C, the response recorded in the magnetic properties of the samples changes again and differs from those of the shorter heating time experiments (4 and 12 hours) and at lower temperatures (above). S-ratio values are barely above those of the unheated control samples on the first episode of heating for 24 hours (88.4 to 89.1). On the second episode, these values reduce (65 to 78). At 48 hours, the S-ratio values are the lowest in the dataset and, like the 24-hour experiments, reduce substantially on the second episode of heating. For example, at 600 °C, the S-ratio is 70.6 on the first episode of heating, reducing to 63.2 on the second. This is due to the inversion of maghemite to haematite, which also accounts for the reduction in MS values (e.g., from 214 to 25 at 600 °C, 24-hour heating time). The magnetic grain size changes from fine SSD to coarse SSD between the first and second episode of heating at 24 hours and is coarse SSD for both heating episodes at 48 hours. At higher temperatures of 900 °C, the results of the 24 and 48 hour experiments are similar to those of the 4 and 12 hour experiments aside from lower χ_{ARM}/SIRM values.

5.7. Experiment 3

The parameter χ_{max} is the maximum possible MS value that the sediment can achieve when subject to heat alteration, which we attained experimentally[37,55]. First, we subjected the unheated control sample to reducing conditions in the furnace (covered for 1 hour at 350 °C) followed by oxidizing conditions (uncovered for 1 hour at 650 °C). This process converts all the iron in the sample to its strongest magnetic form e.g., magnetite/maghemite and thus achieves the highest possible MS value. Chai max or χ_{max} values for the yellowish-brown clayey silt is 549.394 x 10^{-8} m^3/kg^{-1}. Nowhere in any of our heating experiments do we achieve this value.

5.8. Experiment 4

We conducted further experiments to ascertain whether the magnetic properties of the reddened clayey silt could be achieved by increasing the number of successive episodes of heating from 4 up to 12 and 24 times, focusing on the MS and χ_{ARM}/SIRM values which differ in the archaeological samples to those in the first experiments. For experiment 4 we continued with the 4 and 12 hour heating times and at temperatures of 400 and 600 °C. This is because the magnetic mineralogy and grain size of the Area I samples differ substantially to those of the 24 and 48 hour experiments subject to successive episodes of heating at different temperature ranges. For example, S-ratio values reduce to much lower in samples reheated at lower temperatures (300 and 400 °C), and the mineralogy inverts to haematite at higher temperatures > 500 °C on the second episode of heating.

The response of the magnetic properties to a further 12 and 24 successive episodes of heating at temperatures of 400 and 600 °C, and with heating times of 4 and 12 hours are similar (Table 5.4). With 12 successive episodes of heating, there is a reduction in concentration of SP minerals and an assemblage of coarse SSD magnetite grains along with a reduction in the concentration of magnetite. This results in lower MS, χ_{FD}% and χ_{ARM}/SIRM values and S-ratio values relative to experiments 1 and 2. With 24 episodes of heating, we see a further reduction in the concentration of SP minerals and SSD magnetite grains resulting in substantially lower MS χ_{FD}% and χ_{ARM}/SIRM values.

The magnetic properties of the experiment 4 samples still differ from the reddened clayey silt samples (1053 and 1100) in that the MS values are always much higher and the χ_{FD}% values much lower across each experiment. However, the magnetic properties of sample 1054 are similar in grain size and mineralogy e.g., χ_{FD}% and χ_{ARM}/SIRM S-ratio values to the experimental samples heated for 24 times regardless of temperature and duration of heating. That said, the MS value of 1054 is five times lower which may suggest another origin for part of the magnetic assemblage.

5.9. Summary

The results of the experiments show that the magnetic properties of single more extensive heating events with durations of 24 hours and greater, heated to temperatures of 500 and 700 °C, differ from those of relighting events within the same temperature range for periods of 4 and 12 hours. This suggests that in some circumstances magnetic parameters can be used to differentiate between different heating processes in the archaeological record. The inversion of magnetite/maghemite to haematite under conditions of heating longevity is similar to previous results[45] but differs from that observed at Beeches Pit[28]. At Beeches Pit, inversion to haematite only occurred after 4 successive episodes of heating over similar times to heat exposure e.g., 24 and 48 hours. Variation in response of different substrates to heating longevity was also observed in previous experiments[45]. The Barnham and Beeches Pit results further support the effects of time dependency on the magnetic properties of heated sediments and reinforce the need to create experimental reference data sets of the same substrate when conducting any archaeomagnetic fire study using any parameter.

In the Barnham sediments, single more extensive heating events (e.g. 24 hours) result in a mineral magnetic assemblage with a much higher contribution from haematite and a dominance of fine to ultrafine SSD grains or, at 48 hours, a grain size assemblage dominated by coarse SSD grains with mostly haematite. Heating successively for more extensive periods (above 500 °C at both 24 and 48 hours) results in the complete inversion of magnetite to haematite, reflected here in the very low S-ratio values of the experimental data set, and ruling out this process for the archaeological samples which are magnetite dominated with much higher χ_{FD}% values. Single more extensive heating events at lower temperatures, e.g. 300 and 400 °C, also result in higher MS and lower S-ratio values. Reheating of these samples at these temperatures results in a reduction of SP minerals and lower χ_{FD}% values compared with two of the reddened clayey silt samples (1053 and 1100).

The magnetic properties of two reddened clayey silt samples (1053 and 1100) differ from those formed under the heating conditions in the experimental data set and from those of the unheated control samples of the yellowish-brown clayey silt. These reddened clayey silt samples contain large quantities of pyrogenically formed SFMs and SP minerals, yet the MS values do not overlap with any of the experiments and are much lower. The MS values of all the reddened clayey silt samples (1053, 1100 and 1054) are not typical of any MS value obtained in our heating experiments. Similar MS, values produced during heating were only obtained when magnetite/maghemite inverted to haematite during single extensive heating events, successive episodes of heating for 24 and 48 hours and high temperatures of 900° C. In all cases, the mineralogy is always haematite.

Table 5.3. The magnetic properties of the experimental reference data set (experiment 2) created from the yellowish-brown sandy silt for different temperatures 300 to 900 °C, number of successive heating episodes (1-4) and different durations 4, 12, 24 and 48 hours. Experiments were conducted once.

Time	**4 hours**				**12 hours**				**24 hours**				**48 hours**			
No (1-4) °C of heating	**MS**	**χ_{FD}%**	**χ_{ARM}/ SIRM**	**S-ratio**	**MS**	**χ_{FD}%**	**χ_{ARM}/ SIRM**	**S-ratio**	**MS**	**χ_{FD}%**	**χ_{ARM}/ SIRM**	**S-ratio**	**MS**	**χ_{FD}%**	**χ_{ARM}/ SIRM**	**S-ratio**
1. 300	143.423	10.78	0.97	94.615	148.942	10.81	0.96	93.427	124.873	10.74	0.87	91.325	105.318	9.67	0.89	89.451
2. 300	147.961	10.96			151.663	10.92			118.437	9.93	0.81	90.112	98.946	8.18	0.83	88.773
3. 300	149.328	10.98			153.448	10.96										
4. 300	151.668	10.99	0.92	92.996	155.407	11.01	0.93	92.498								
1. 400	224.151	10.94	0.99	97.163	232.425	11.01	1.01	98.162	167.346	10.75	0.88	92.486	84.561	10.54	0.88	85.453
2. 400	231.607	11.03			235.639	11.12			124.156	8.42	0.8	90.629	64.92	8.52	0.73	83.691
3. 400	232.118	11.09			237.437	11.24										
4. 400	235.222	11.14	0.95	95.639	239.958	11.31	0.95	96.476								
1. 500	262.305	11.43	0.88	97.848	281.994	11.86	0.91	97.592	210.231	11.11	0.91	88.461	34.523	9.41	0.53	71.326
2. 500	294.301	11.57			301.482	12.4			40.82	7.03	0.29	78.419	10.847	4.09	0.23	64.739
3. 500	297.629	11.64			307.348	12.51										
4. 500	299.537	11.68	0.83	96.107	314.012	12.58	0.84	96.623								
1. 600	266.427	12.64	0.8	97.458	294.471	12.89	0.85	98.453	214.629	11.94	0.94	89.163	32.628	8.98	0.51	70.672
2. 600	269.387	12.68			307.885	13.1			25.383	8.15	0.34	70.597	9.274	4.46	0.21	63.292
3. 600	271.484	12.94			311.443	13.21										
4. 600	274.632	12.98	0.78	95.739	315.849	13.24	0.81	97.365								
1. 700	238.727	11.07	0.73	98.429	245.823	11.37	0.76	98.922	197.334	10.93	0.74	89.035	29.473	7.95	0.54	69.962
2. 700	242.634	11.54			249.616	11.94			44.85	7.87	0.23	65.632	10.831	4.98	0.21	60.427
3. 700	243.873	11.58			251.449	11.98										
4. 700	243.941	11.6	0.71	97.118	254.663	12.01	0.75	97.707								
1. 900	44.58	5.74	0.72	77.657	41.236	5.62	0.71	77.115	22.183	5.12	0.69	73.48	15.183	4.32	0.52	73.927
2. 900	43.049	5.32			39.476	5.31			15.3	4.41	0.21	60.361	12.981	3.98	0.21	60.334
3. 900	41.427	5.31			37.44	5.25										

Table 5.4. Magnetic properties for experiment 4 with samples reheated for 12 and 24 successive episodes of heating for 4 hours and then 12 hours at temperatures of 400 and 600 °C. Experiments were conducted once.

4-Hour experiments (No. heating and temp °C)	MS or χ_{LF} $10^{-8}m^3kg^{-1}$	χ_{FD}%	S-ratio	χ_{ARM}/SIRM $10^{-3}mA^{-1}$	12-Hour experiments (No. heating and temp °C)	MS or χ_{LF} $10^{-8}m^3kg^{-1}$	χ_{FD}%	S-ratio	χ_{ARM}/SIRM $10^{-3}mA^{-1}$
12. 600	213.45	9.42	93.56	0.68	12. 600	225.37	9.49	94.46	0.68
12. 400	193.25	8.92	92.26	0.73	12. 400	201.32	9.25	92.29	0.74
24. 400	78.90	8.12	91.91	0.59	24. 400	71.03	7.96	91.49	0.56
24. 600	72.40	8.03	92.36	0.56	24. 600	70.45	7.84	92.04	0.54

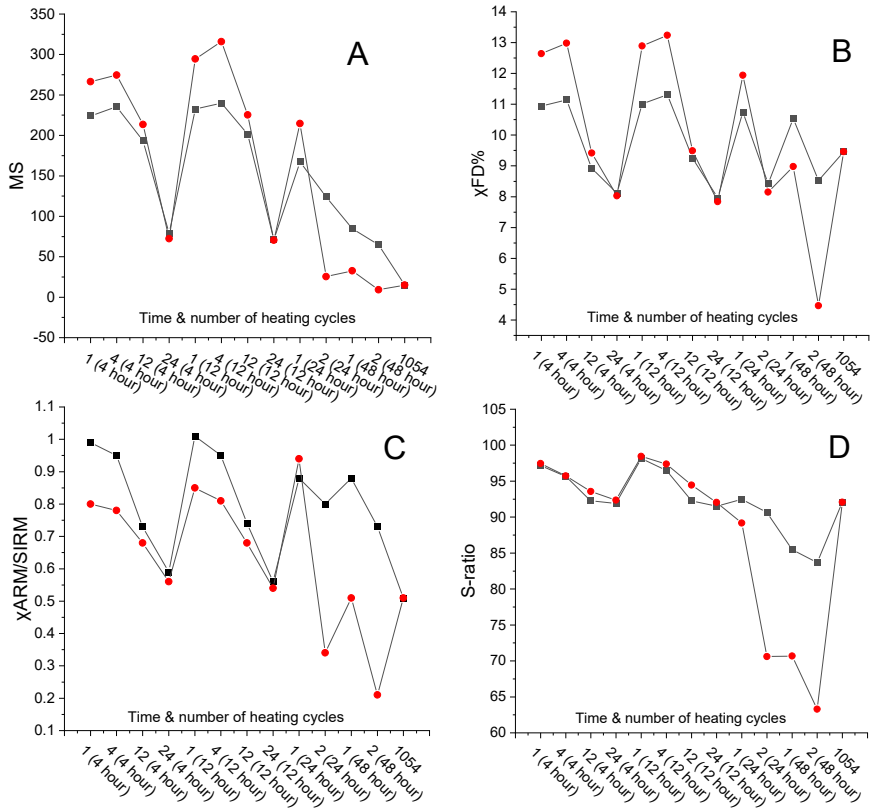

Figure 5.2. shows the magnetic properties of the samples from Table 5.4 as compared to sample 1054 from Area 1. On the y-axis and specific to each plot - **A.** is the magnetic susceptibility (MS), **B.** χ_{FD}%, **C.** χ_{arm}/SIRM and **D.** S-ratio. The x axis on all plots shows the number of heating cycles the samples were exposed to 1 – 24 and the duration of the heating experiment in hours in brackets. The black and red symbols denote the temperature of heating in 400 and 600 °C respectively.

It is likely that all the reddened clayey silt samples contain a mix of heated and non-heated magnetic minerals caused by diffusion of either heated or unheated minerals in the matrix of the deposit resulting in a magnetic assemblage of pyrogenically formed SFMs which enhanced the weakly magnetic surrounding materials[39]. The FTIR and micromorphology results further support this interpretation. There is some indication of relighting in that the magnetic properties of 1054 could be similar to those of relighting events e.g., similar χ_{FD}% and χ_{ARM}/SIRM S-ratio values to experiment 4. However, as the MS value may indicate materials of variable origins, it cannot be conclusively determined, and we put this forward as a suggestion.

6. Polycyclic aromatic hydrocarbons

Sally Hoare

6.1. Examining prehistoric fire use using PAH

PAHs serve as biomolecular records for fire providing quantitative data on its natural occurrences and patterns in various environments across geological timescales[56,57]. The PAHs produced during burning have different structures of 2 to 6 rings. Previous research has shown that the production of PAHs varies when wood is burned, with those having a lower molecular weight (less than 4 rings, lPAHs) found predominantly in the gaseous phase, and those with a higher molecular weight (more than 4 rings, hPAHs) found in the particulate phase[58,59]. Archaeological evidence indicates that anthropogenic combustion features can reach sufficiently high temperatures to generate hPAHs[60,61], whereas natural fires in different settings and intensities consistently show a higher lPAH:hPAH ratio in soils and sediments[62-64]. It is suggested that the higher hPAH:lPAH ratio in archaeological sites is due to wood burning in the immediate area (10s of m), as hPAHs are part of the particulate emission phase and less prone to travel far from the fire's origin[62,65]. It is further suggested that greater concentrations of lPAHs in sediments at archaeological sites are due to the long-distance spread of natural fires, while hPAHs would be more concentrated due to the local deposition of particles from wood burning, whether from human activities or nearby forest fires. Thus, research suggests that a higher ratio of hPAHs to lPAHs could indicate human fire use at some archaeological locations[28,65].

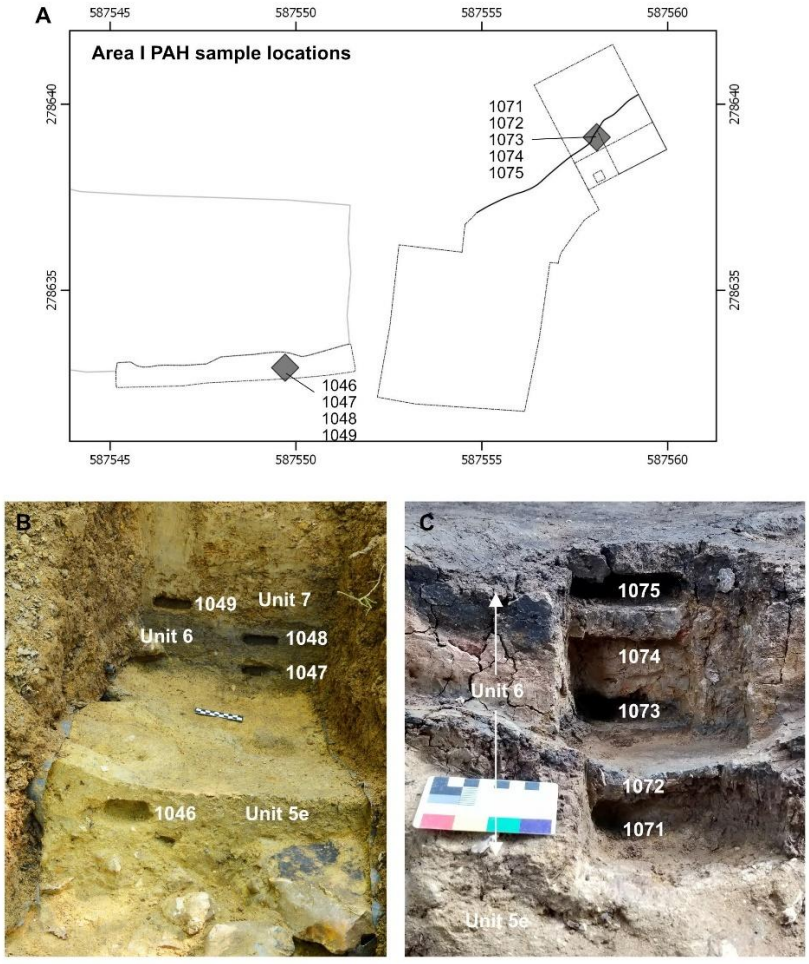

Figure 6.1. Locations (**A**) of sediment samples taken for PAH analysis from Area I West (**B**) and Area I East (**C**).

6.2. Sampling on site

Nine samples were collected from Area I in by RD in 2022 (Fig. 5.1 and Table 5.1) using sterilised equipment following previous procedures[65,66], transported in a portable freezer to the University of Liverpool, and placed immediately into a lab freezer at -20 °C. Two control samples were taken by SH from sediments affected by recent wildfires within the site catchment of (Thetford Forest) to act as control samples and to compare both the (PAH) distributions and their statistical relationships[28].

6.3. Methods

Ten grams of ultrasonically dispersed sediment samples were mixed with recovery standards to measure and quantify the efficiency of analytical methods. The samples were then Soxhlet extracted for 24 h using a 200 mL mixture of hexane and dichloromethane (1:3, v:v). The sediment extract was concentrated to 4 mL using a rotary evaporator and purified with a silica gel and alumina column (2:1, v:v; 30 cm height ×10 mm i.d.) with He as the carrier (1.5ml/min). Each column containing the target PAHs was eluted with 70 mL of hexane and dichloromethane mixture (7:3, v:v), concentrated to 0.5 mL and spiked with internal standards before instrumental analysis. The total concentrations of the PAHs in the solutions were determined by gas chromatography mass spectrometry (GC-MS Agilent 7890A GC equipped with 5977B Mass-Selective detector) and using a 30 m DB-5MS fused silica capillary column (0.25 mm i.d., 0.25 mm film thickness). The oven temperature was ramped from 60 to 200 °C for 10 °C/min, and then to 214 °C for 2 °C/min, then to 254 °C for 5 °C/min and finally to 290 °C for 18 °C/min. The temperature was held for 2 min at 254 °C and 17 min at 290 °C. Calibration standards and spiked and procedural blanks were included with every 10 samples to ensure quality assurance and control. Samples were analysed using a 16 component PAH standard (PAH mix 6) at known concentrations ranging from 0.25 to 400 ng for calibration and quantification (standard error 4%). Normalisation relative to the dry weight of extracted sediment was used to normalize PAH concentrations in the samples, which is the most common approach, established to reduce potential effects of changes in sediment particle size distribution on PAH abundances[65,67,68].

Table 6.1. Stratigraphy of sediments sampled for PAH analysis in Area I West (described in the field as upper and lower palaeosol) and Area I East.

Stratigraphy	Area I West			Area I East	
	Deposit	Sample no.		Deposit	Sample no.
Unit 7	Brickearth	1049			
Unit 6	Palaeosol (upper)	1048		Upper black clayey silt	1075
				Reddened clayey silt	1074
	Palaeosol (lower)	1047		Yellowish-brown clayey silt	1073
				Lower black clayey silt	1072
				Brown clayey silt	1071
Unit 5e	Yellow silty sand	1046			

6.4. Origin of the PAH assemblages

Seven low ring and five high ring PAHs were detected in the sediments (Table 6.2). Some ratios of low ring PAHs can be used to determine whether their origin is pyrolytic and whether the source of the pyrolysis is wood combustion or petroleum (Table 6.3). The ratio of Phe/Ant < 10 can be used to determine whether the source of the PAHs is pyrolytic in origin[69], which is the case for all the Barnham samples. The ratios of Fla/(Fla + Pyr) > 0.5 and BaA/(BaA+CHR) > 0.4 can be used to further

determine the source of the pyrolysis, either petroleum or grass, wood and coal[66,70]. Both ratios indicate that the source of the pyrolysis is from the combustion of grass, wood or coal.

Table 6.2. Low ring and high ring PAHs in the Barnham samples (Ip- Indeno(1,2,3-cd)pyrene and Da-Dibenzo(a,h)anthracene were combined and are listed as ([Ip,Da]*a).

Low ring lPAH	**High ring hPAH**
Flourene **(Fle*)**	Benzo(b)fluoranthene **(B(b)f*)**
Phenanthrene **(Phe*)**	Benzo(k)fluoranthene **(B(k)f*)**
Anthracene **(Ant*)**	Benzo(a)pyrene **(B(a)p*)**
Flouranthene **(Fla*)**	Indeno(1,2,3, cd)pyrene **([Ip,Da]*a)**
Pyrene **(Pyr*)**	Benzo(g,h,i)perylene **(B(g,h,i)p*)**
Benz(a)anthracene **(B(a)a*)**	
Chrysene **(Chr*)**	

Table 6.3. The abundances of PAHs in the Barnham sediments in Area I as ratios of Phen/ANT, FLT/FLT+PYR and BaA/BaA + CHR, with abundances of hPAH to lPAHs. Sediments with a higher ratio of hPAHs to lPAHs are marked in bold. Control samples (TF KLF A and TF 2A) from recent wildfires in Thetford Forest are also shown.

Sample code	**Sediment (unit)**	**Phen/ANT**	**FLT/(FLT + PYR)**	**BaA/(BaA + CHR)**	**hPAH**	**lPAH**	**Interpretation**
1075	Upper black clayey silt (6)	9.19	0.48	0.58	32.02	249.56	Regional fires
1074	Reddened clayey silt (6)	7.06	0.55	0.66	**253.56**	**167.88**	Repeated human fire use
1073	Yellowish-brown clayey silt (6)	8	0.5	0.69	16.24	150.49	Regional fires
1072	Lower black clayey silt (6)	6.33	0.45	0.6	33.12	146.96	Regional fires
1071	Brown clayey silt (6)	7.98	0.5	0.69	16.28	149.72	Regional fires
1049	Brickearth (7)	6.79	0.53	0.73	9.28	45.27	Regional fires
1048	Palaeosol (upper) (6)	9.08	0.48	0.58	32	248.83	Regional fires
1047	Palaeosol (lower) (6)	9.43	0.48	0.58	27.47	244.57	Regional fires
1046	Yellow silty sand (5e)	6.46	0.61	0.59	15.98	38.61	Regional fires
TF KLF A		7.7	0.52	0.56	38	222.5	Wildfire
TF 2A		8.6	0.55	0.76	52.7	246.1	Wildfire

Table 6.4. The low-ring and high-ring PAH distributions for samples from Area I, Barnham, and two from recent wildfires in Thetford Forest (TF KFL A and TF 2 A).

Sample code	**Fle**	**PHE**	**ANT**	**Fla (flt)**	**PYR**	**BaA**	**CHR**	**BbF**	**BkF**	**BaP**	**[Ip,Da]*a**	**BghiP**
1075	33.25	114.93	12.51	32.22	34.64	12.81	9.2	11.4	1.91	11.14	1.36	6.21
1074	24.01	76.43	10.83	23.01	19.11	9.62	4.87	42.93	53	140.47	16.14	1.02
1073	23.83	75.92	9.49	16.45	16.34	5.82	2.64	5.58	1.11	6.04	0.71	2.8
1072	30.45	50.21	7.93	22.65	28.04	4.58	3.1	5.21	0.91	8.21	15.67	3.12
1071	23.23	75.61	9.47	16.39	16.64	5.79	2.59	5.61	1.14	6.11	0.73	2.69
1049	1.2	13.52	1.99	11.41	10.01	5.18	1.96	4.92	0.72	2.26	0.61	0.77
1048	33.29	113.99	12.55	32.24	34.74	12.72	9.3	11.41	1.87	11.16	1.38	6.18
1047	32.14	113.03	11.98	31.27	33.81	12.94	9.4	10.55	1.68	10.74	1.27	3.23
1046	1.15	10.79	1.67	10	6.36	5.13	3.51	5.21	2.72	1.64	3.27	3.14
TF FKL A	26	126.5	16.3	24.9	22.4	3.6	2.8	19.3	2	5.9	5.6	5.2
TF 2A	47.4	132.2	15.3	24.1	19.5	5.8	1.8	9.7	2.7	14	21.8	4.5

6.5. Results

The total abundance of hPAHs and lPAHs were analysed with one sample from unit 5e, seven from unit 6, and one from unit 7 (Tables 6.1, 6.3). Samples 1046 (unit 5e) and 1049 (unit 7) preserve higher ratios of lPAHs to hPAHs, which is also the case for samples 1075, 1073, 1072, 1071, 1048 and 1047 from the yellowish-brown clayey silt and brown clayey silt in unit 6. By contrast, sample 1074 (reddened clayey silt), preserves a higher abundance of hPAH to lPAHs, with the abundances of hPAHs ordered from highest to lowest B(a)p > B(k)f > B(b)f > Ip,Da > B(g,h,i)p (Table 6.4).

Statistical analysis. Pearsons r and linear regression was performed using Origin Pro 2020 to further investigate the relationship between localised wood combustion in the immediate vicinity of the site (hPAH) and natural fires at the regional scale (lPAH). The results show that some of the lPAHs have a moderate to strong statistical correlation with the hPAHs in the Barnham data set. This may suggest some link between the occurrence and frequency of fires in the immediate vicinity of the site and natural fires occurring at a more regional scale. The strongest correlation is between the lPAHs (Fle, Phe, Fla, Pyr, BaA and CHR) and hPAH, (BghiP), being r = (0.58, 0.63, 0.68, 0.70, 0.61 and 0.73) respectively. These statistical relationships were further examined using linear regression analysis. BghiP shows a strong statistical correlation with other hPAHs in the two controls samples taken from recent wildfires in Thetford Forest and is good indicator of links between hPAH and lPAH distributions in natural fires[28]. The results (Fig. 6.2.A-F) show that the statistical correlation is only strong for some of the samples in the data set, those which fall close to the regression line and are statistically significant at < p 0.05 on Fig 6.2. C, D and F. Samples 1048 and 1075 from the upper black clayey silt, and samples 1071 and 1073 from the brown clayey silt and yellowish-brown clayey silt respectively, show strong relationships between BghiP and Fle, Phe, Fla, Pyr and BaA. Sample 1072 from the lower black clayey silt shows a strong relationship between BghiP and Fla. The brickearth sample also shows a strong relationship between BghiP and Fla, Pyr, BaA and Chr. All these samples preserve higher abundances of lPAHs to hPAHS. Sample 1074 is the only one to preserve a higher hPAH abundance in the data set, and falls away from the regression line on all plots, showing no statistical correlation with any of the lPAHs in the total assemblage including plots 6.2 C, D and F.

6.6. Summary

Only one sample (1074) preserves a higher abundance of hPAH to lPAHs. The hPAH abundance is ordered highest to lowest from B(a)p > B(k)f > B(b)f > Ip,Da > B(g,h,i)p. The ordering of the hPAHs is similar to both local wood burning and archaeological studies in which the distribution was demonstrated to be representative of human fire use and the potential for independent ignition[28,65,71-73]. The reddened clayey silt (1074), is potentially altered via heat from the yellowish-brown clayey silt (1073). However, the data in Tables 6.3 and 6.4 show that its PAH assemblage differs from the latter sample in terms of overall PAH abundances. Furthermore, the lPAH abundance does not decrease in 1074 relative to 1073, showing that post-depositional processes could not have affected the PAH assemblage and could not have resulted in a higher concentration of hPAHs in this sample. The linear regression analysis (Fig. 6.2A-F) shows that sample 1074 falls away from the regression line on all plots, but also that it is not close to the other sample from the same sedimentary unit. This suggests a different source for the PAH assemblage of 1074 relative to 1073. There is also no statistical link between any of the hPAHs and lPAHs in the reddened clayey silt, whereas the sample from the yellowish-brown clayey silt falls close to the regression line on plots A to E (Fig. 6.2). The two possible explanations are, first that there is a decoupling of the relationship between the occurrence of natural fires locally and regionally in 1074 but not in 1073. Or second, the hPAH abundance indicates human use and control of fire at Barnham which occurs independently from the incidence of natural fires at the regional scale. Samples 1075, 1047 and 1048 preserve the

highest abundance of lPAHs in the data set which may indicate that there is an increase in frequency or intensity of regional fires over time, and during the formation of the upper black clayey silt.

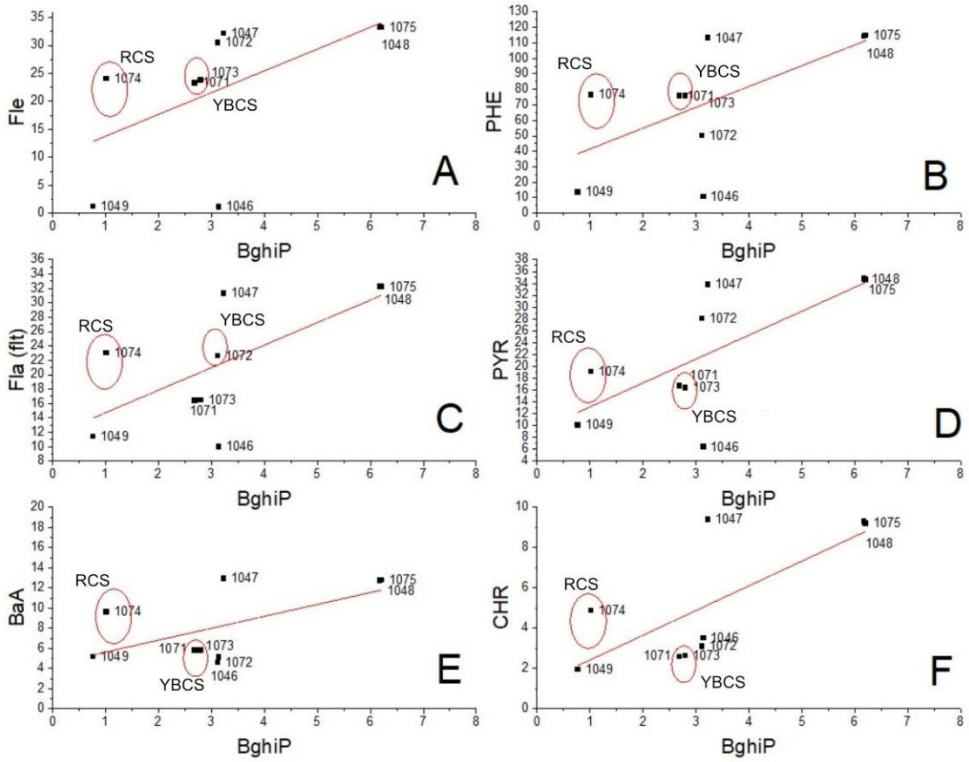

Figure 6.2. Linear regression analyses showing the relationship between hPAH (BghiP) and lPAH (Fle, PHE, Fla, Pyr, BaA and CHR) shown on plots A to F. The sample from the reddened clayey silt, preserving a higher abundance of hPAH relative to lPAH, I is shown in the red circle. The unaltered substrate for this sample, the yellowish-brown clayey silt, is also marked on plots A to E. Statistical analysis was performed using Origin Pro (Table 6.5) number of samples (n=9). Standard error was scaled with square root of reduced Chi Sqr and the slope was significantly different from zero at the 0.05 level on plots C, D, and F only. The p values for these plots were C (p 0.04), D, (p 0.03) and F (p 0.02).

Table 6.5. Statistics from Origin Pro for each plot in Figure 6.2.

	Plot A	**Plot B**	**Plot C**
Equation	y = a + b*x	y = a + b*x	y = a + b*x
Plot	Fle	PHE	Fla (flt)
Weight	No Weighting	No Weighting	No Weighting
Intercept	9.88623 ± 7.63158	28.03257 ± 22.85331	11.58364 ± 4.71821
Slope	3.89485 ± 2.06023	13.44777 ± 6.16949	3.13399 ± 1.27373
Residual Sum of Squares	862.06804	7730.55674	329.50863
Pearson's r	0.58138	0.63586	0.681
R-Square (COD)	0.338	0.40432	0.46376
Adj. R-Square	0.24343	0.31922	0.38716
	Plot D	**Plot E**	**Plot F**
Equation	y = a + b*x	y = a + b*x	y = a + b*x
Plot	PYR	BaA	CHR
Weight	No Weighting	No Weighting	No Weighting
Intercept	9.10166 ± 5.70584	4.45149 ± 2.15191	1.19789 ± 1.60178
Slope	4.03893 ± 1.54035	1.18404 ± 0.58093	1.22733 ± 0.43242
Residual Sum of Squares	481.89499	68.54262	37.97676
Pearson's r	0.70392	0.61027	0.73148
R-Square (COD)	0.49551	0.37243	0.53507
Adj. R-Square	0.42344	0.28278	0.46865

7. Fourier-transform infrared spectroscopy

Marcus Hatch and Simon Lewis

7.1. Stepwise incremental heating experiment

For the FTIR heating experiments, sample 1084 was taken from the yellowish-brown clayey silt adjacent to the sampling column in Area I East, as 'parent' material for the reddened clayey silt. The aim was to provide a reference collection of FTIR wavelength responses to heating at known temperatures. Initial analysis of Area I sediments (Figure 7.1) shows that sample 1084 exhibits the same clay peaks as samples from the purported fire feature and provides suitable reference material for the heating experiment. Based on previous studies[74-76] and preliminary laboratory work, it was expected that alterations due to heating would be detected in changes to kaolinite clay bands around the 1035 cm^{-1}, 915 cm^{-1} and 533 cm^{-1} wavelength regions. The heating experiment was designed to determine the temperature of those alterations to construct a spectra library specific to the sediments at Barnham. Previous experimental work has shown that sediments containing different clay types produce different temperature responses, and so the use of local sediments to construct site-specific spectra libraries is essential[75].

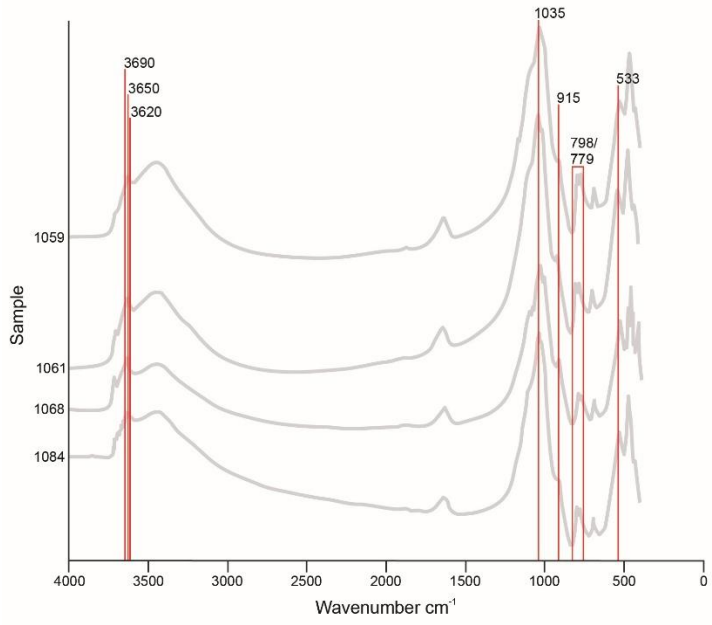

Figure 7.1. Characterisation of the minerology of unaltered sediments as shown by FTIR. Sample 1084 shows diagnostic kaolinite peaks at 3690 cm^{-1}, 3650 cm^{-1}, 3620 cm^{-1}, 1035 cm^{-1}, 915 cm^{-1} and 533 cm^{-1}. The quartz doublet at 797 cm^{-1} and 779 cm^{-1} is also visible. Sample 1068 (brown clayey silt), sample 1061 (reddened clayey silt/yellowish-brown clayey silt) and sample 1059 (upper black clayey silt/reddened clayey silt) show the same kaolinite peaks and also appear not to have been heated sufficiently to be altered.

7.2. Methods

The heating experiment was carried out using subsamples of 1084. Each sample was heated in a porcelain crucible in a muffle furnace for 4 hours, at temperatures ranging from 250 to 1000 °C in 50 °C increments. A further two samples were heated to 150 and 200 °C in a laboratory oven for convenience. An unheated (oven-dried to 105 °C) sample was prepared for reference. Samples for both the heating experiment and FTIR analysis of the archaeological samples (see below) were prepared by grinding ~2-3 mg of sample in an agate mortar and pestle and mixing with 200 mg of potassium bromide (KBr). ~80 mg of the mixture was then formed into a transparent disc using a

hand press. A Thermo Nicolet iS10 spectrometer was used to analyse the samples and obtain spectra between 4000 cm^{-1} and 400 cm^{-1}, at 4 cm^{-1} intervals. The FTIR reference collection of standard materials created by the Kimmel Center of Archaeological Science, Weizmann Institute of Science[77] was used for comparison with the Barnham sample spectra.

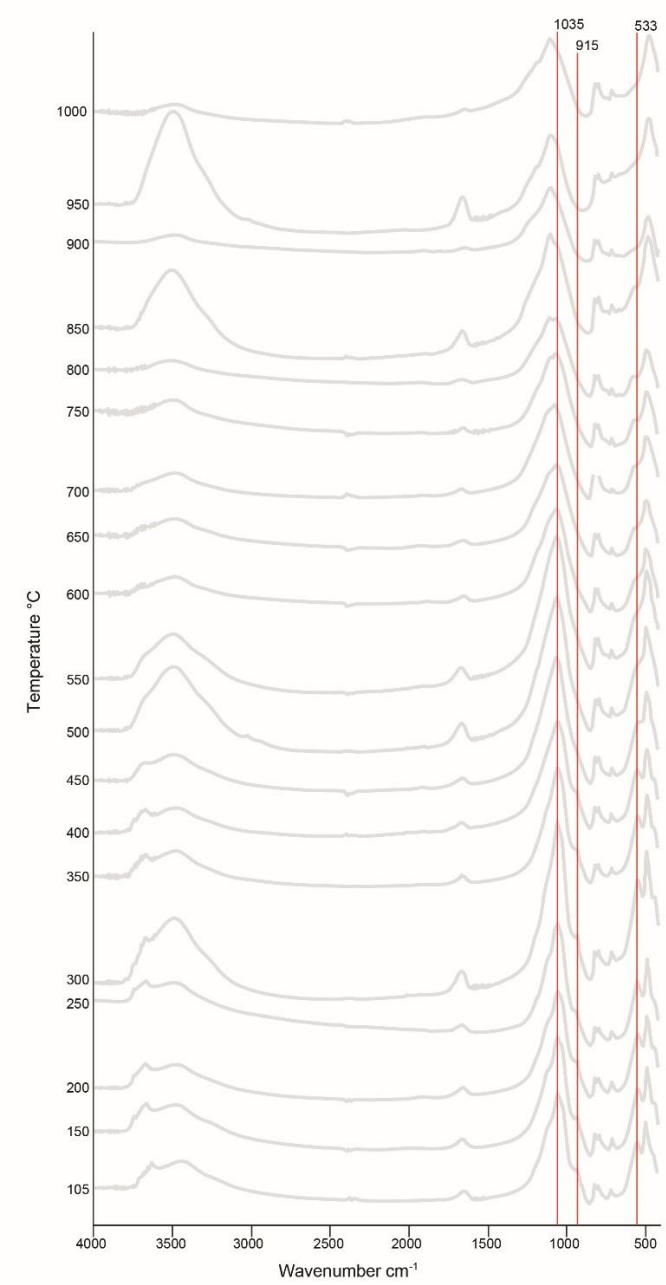

Figure 7.2. Infrared spectra of sample 1084 heated in a muffle oven for four hours at temperatures between 105 and 1000 °C. As temperature increases above 450 °C there is a shift of the dominant peak from wavenumber 1035 cm^{-1} towards 1085 cm^{-1}. The spectra also show the reduction and disappearance of the peak at 915 cm^{-1} above 350 °C and the shift and disappearance of the peak at 533 cm^{-1} above 500 °C.

7.3. Heating experiment results

Interpretation of the response to increasing temperatures in the heating experiment focused on three wavelength regions characteristic of absorption bands in clays: 1035 cm^{-1}, 915 cm^{-1}, and 533 cm^{-1}, indicating Si-O stretch, OH deformation and Si-O-Al stretch respectively[74,76]. Other significant

clay bands are seen at 3690 cm^{-1}, 3650 cm^{-1} and 3620 cm^{-1}, while other bands show the presence of quartz, as seen by the peak at 1085 cm^{-1}, the double peak at 797/779 cm^{-1} and the peak at 694 cm^{-1}.

The spectra and wavelength changes produced by the heating experiment (Figs 7.2 and 7.3, Table 7.1) show no significant changes between 105° and 300°. The major clay band is largely stable at around 1035 cm^{-1}, and there are strong peaks at 915 cm^{-1} and 533 cm^{-1}. At 450 °C the 1035 cm^{-1} peak begins to shift to higher wave numbers (Figs 7.2 and 7.3A); between 450 and 750 °C the shift is seen to ~1042-1047 cm^{-1}, while from around 600 °C the quartz band at 1085 cm^{-1} becomes visible. From 800 °C the 1085 quartz peak is dominant in the region. At 350 °C the peak at 915 cm^{-1}, previously clearly visible, is diminished (Fig. 7.2). From 400 °C the 915 cm^{-1} peak is absent. The 533 cm^{-1} peak is stable up to 400 °C (Figs 7.2 and 7.3B), then the peak shifts to from 540 to 553 cm^{-1} as temperature increases between 500 and 850 °C. From 900 °C the peak is absent.

Table 7.1. Numeric values for wavelength changes during the heating experiment on the Barnham samples after heating between 105 and 1000 °C alongside a summary of those changes.

Temperature	**1035 cm^{-1} region**	**915 cm^{-1} peak**	**533 cm^{-1} region**	**Summary**
105°	1034.82	915.03	533.28	**1035 cm^{-1} peak**
150°	1038.68	915.29	532.67	Stable at 105°-350°/400°
200°	1034.89	915.40	533.21	Shift to higher wavenumbers at 450°-750° (~1042-1047 cm^{-1})
250°	1034.88	915.59	533.05	Appearance of peak ~1085 cm^{-1} between 550°-750°
300°	1034.77	915.30	533.32	1085 cm^{-1} peak dominant between 800°-1000°
350°	1034.97	918.94	533.17	
400°	1038.54	None	533.40	**915 cm^{-1} peak**
450°	1042.38	None	536.59	Visible at 105°-300°
500°	1046.37	None	540.42	Diminished at 350°
550°	1046.28	None	546.01	Absent at 400° and above
600°	1046.72	None	None	
650°	1046.30	None	541.24	**533 cm^{-1} peak**
700°	1046.29	None	542.40	Stable at 105°-400°
750°	1046.66	None	551.09	Shift to higher wavenumbers (540 to 553 cm^{-1}) at 500°-850°,
800°	1084.88	None	553.47	with peak magnitude significantly reduced
850°	1085.01	None	548.55	Peak absent at 900° and above
900°	1085.21	None	None	
950°	1084.72	None	None	
1000°	1085.21	None	None	

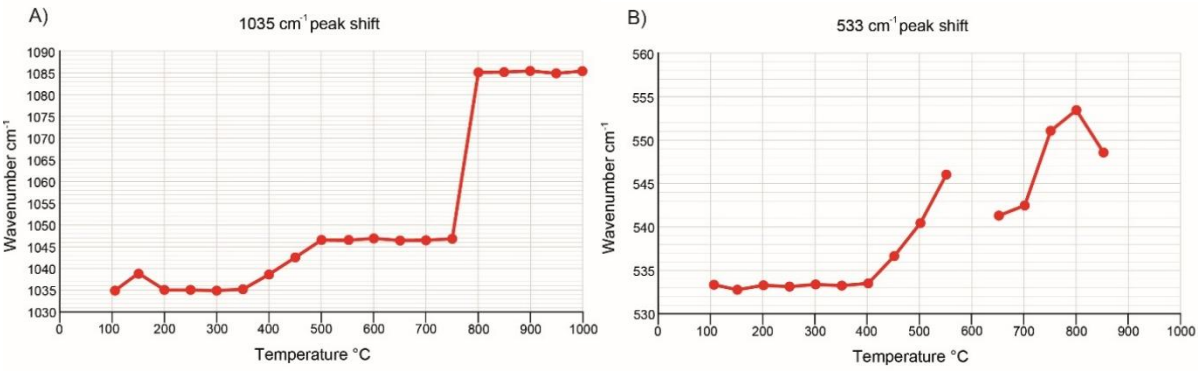

Figure 7.3. A. The shift of the major clay peak at 1035 cm^{-1} and the development of the quartz peak at 1085 cm^{-1}, and **B.** the shift of the 533 cm^{-1} peak as shown in the heating experiment on the Barnham samples. Note at 600 °C the reduced peak in the 533 cm^{-1} region was insufficient to register.

7.4. Archaeological samples and results

A column of nine samples was taken in a section through the purported fire feature in Area I East. These incorporated the upper black clayey silt, reddened clayey silt, yellowish-brown clayey silt, lower black clayey silt and brown clayey silt. Once in the laboratory each sample was examined for visually reddened sediments, which were present to a greater or lesser degree in each sedimentary unit and each sample. These reddened sediments were then preferentially selected for FTIR analysis.

Of the nine samples analysed, five showed evidence of heat alteration (Fig. 7.4, Table 7.2). Sample 1057 is consistent with being heated to around 400 °C: the shift in the major clay band to 1039/1046 cm^{-1} indicates temperatures between 400 and 500 °C, while the 915 cm^{-1} peak is just absent, suggestive of 350-400 °C. The unaltered 533 cm^{-1} peak shows that temperature did not reach 450 °C. Sample 1058 appears to indicate being heated to at least 750 °C as seen in the dominant quartz peak at 1085 cm^{-1}, but less than 800 °C as the major clay band is still visible. The absence of a peak in the 533 cm^{-1} region is indicative of temperatures greater than 900 °C but the presence of a peak around 507-513 cm^{-1} may signify a slightly different mineral content. The major clay band in sample 1067 shifted to 1039 cm^{-1}, indicative of heating to around 400 °C, although a dominant quartz peak is also seen at 1077 cm^{-1}. Again the 915 cm^{-1} peak suggests a temperature of 350°-400° and the minor 533 cm^{-1} peak a temperature of 400-450 °C. Similarly, sample 1060 has an unaltered major clay band indicative of heating to less than 400 °C but a dominant quartz peak at 1089 cm^{-1}. The 915 cm^{-1} peak suggests a temperature of 350 °C and the minor 533 cm^{-1} peak suggests one of 400-450 °C. The major clay band in sample 1063 shifted to 1039 cm^{-1}, indicative of heating to around 400 °C while the shift in the 533 cm^{-1} peak indicates ~450 °C. The 915 cm^{-1} peak suggests a temperature of between 350 and 400 °C.

Table 7.2. Temperatures indicated in the three wavelength regions of column samples taken through the purported fire feature in Area I East and interpretation of temperature ranges to which samples were exposed.

Sample	Context	Col.	1035 cm^{-1} peak	915 cm^{-1} peak	533 cm^{-1} peak	Interpretation
1057	Upper black clayey silt	1	400°-500°	350°-400°	<450°	**400°-750°**
1058	Upper black clayey silt	2	~750°	>450°	?>900°	**>750°**
1059	Upper black clayey silt/reddened clayey silt	3	Unaltered [≤350°]	Unaltered [≤300°]	Unaltered [≤400°]	Unheated [≤300°]
1067	Reddened clayey silt	4	~400°	350°-400°	400°-450°	**400°-750°**
1061	Reddened clayey silt/ Yellowish-brown clayey silt	5	Unaltered [≤350°]	Unaltered [≤300°]	Unaltered [≤400°]	Unheated [<300°]
1060	Yellowish-brown clayey silt	6	<400°	~350°	400°-450°	**<400°**
1062	Yellowish-brown clayey silt	7	Unaltered [≤350°]	Unaltered [≤300°]	Unaltered [≤400°]	Unheated [≤300°]
1063	Yellowish-brown clayey silt/ Lower black clayey silt	8	~400°	350°-400°	~450°	**400°-750°**
1068	Brown clayey silt	9	Unaltered [≤350°]	Unaltered [≤300°]	Unaltered [≤400°]	Unheated [≤300°]

Samples 1057, 1058, 1060 and 1063 retain minor absorbance bands at 3621/3630 cm^{-1} and 3691/3696 cm^{-1}. Following previous work[78], this would indicate an admixture of unheated sediment present in samples 1057 and 1063, while in samples 1058, 1060 and 1067 the peaks are reduced, indicating slightly less unheated sediment present. Only sample 1067 loses the 3691/3696 cm^{-1} band completely. Four of the five samples interpreted as being heated (1057, 1058, 1063 and 1067)

showed a shift in the major clay band (1035 cm^{-1} to 1039 cm^{-1} or above) and the loss of the 915 cm^{-1} peak, indicating that any admixture has a minimal effect on the interpretation of temperature reached as shown in the heating experiment. Sample 1060 may also be considered to give a reliable result as the 915 cm^{-1} peak is greatly reduced, but also contains unheated material.

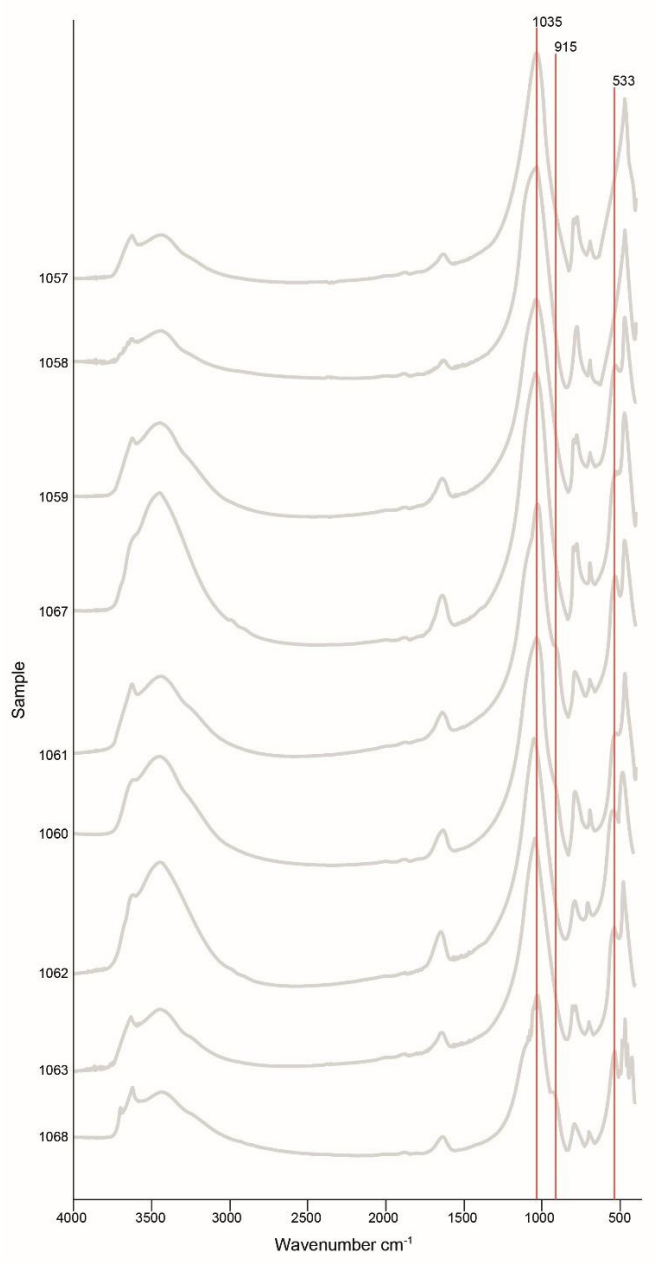

Figure 7.4. Infrared spectra of nine samples taken in a section through the purported fire feature in Area I East.

In summary, analysis of the three wavelength regions characteristic of absorption bands in clays (1035 cm^{-1}, 915 cm^{-1}, and 533 cm^{-1}) in the archaeological samples from Area I, when compared to the heating experiment results, shows reasonable agreement in their respective responses to increasing temperatures (Table 7.2). Two minor anomalies remain: the sample with the least agreement in the responses of the three regions is 1060, but this may be the sample with the most unheated content as discussed above. Finally, sample 1058 lacks the 533 cm^{-1} absorption band, indicating heating of more than 900 °C according to the heating experiment. However, the appearance of a peak at ~510 cm^{-1}, likely to be a quartz band[77] could be masking what would be a minor peak at ~550 cm^{-1} as seen

in the heating experiment at 750 °C. In this case the likely temperature reached, as indicated by the major clay band of the sample, would be ~750 °C. Finally, samples 1059, 1061, 1062 and the basal 1068 appear to be unheated. Taken together, the three wavelength regions studied allow the grouping of sediments at Barnham Area I into four broad categories – unheated (≤300 °C), and heated to <400 °C, 400 to 750 °C and >750 °C (Table 7.2). These results are consistent with those from the magnetic studies.

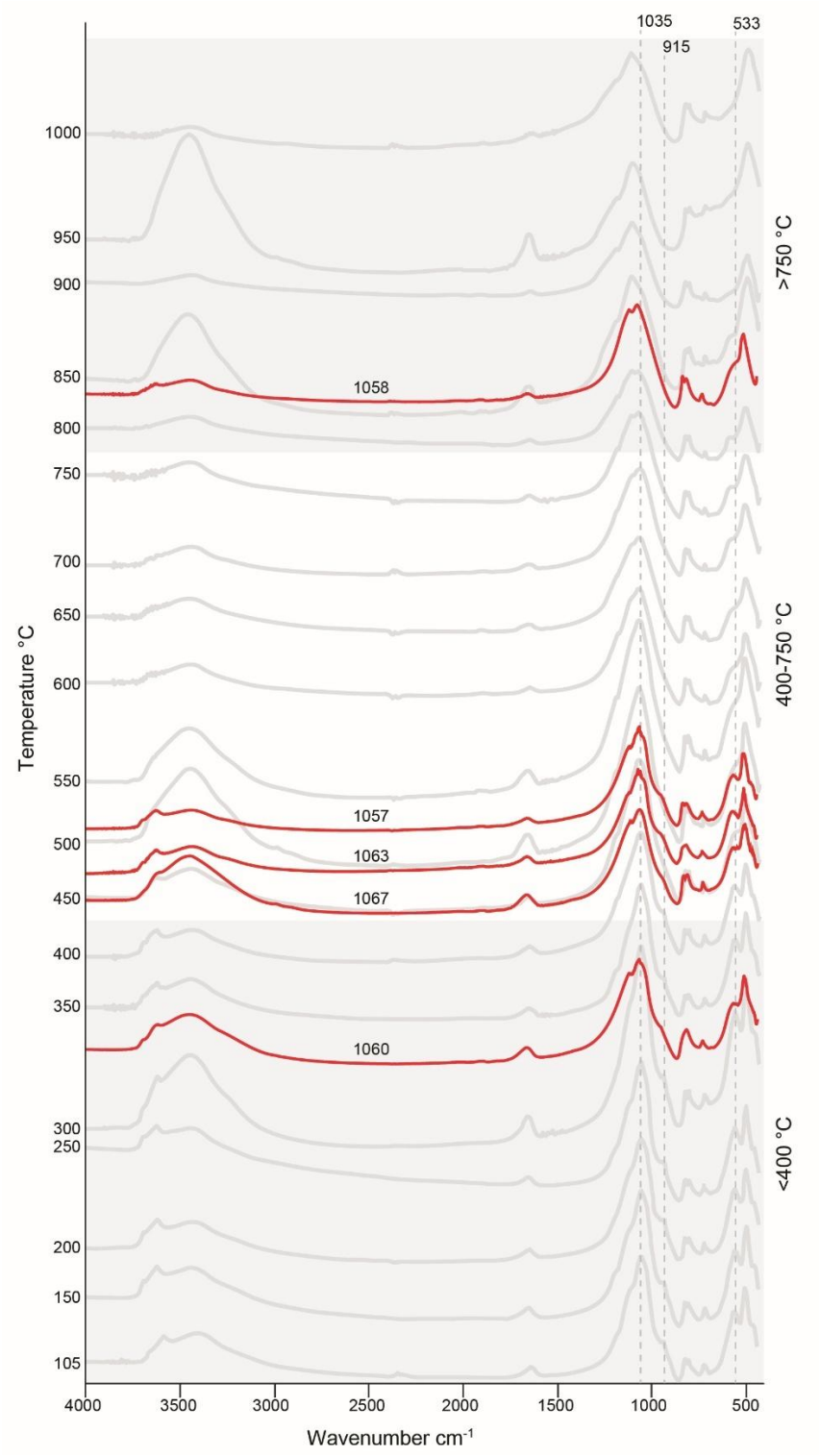

Figure 7.5. Comparison of the three wavelength regions characteristic of absorption bands in clays (1035 cm^{-1}, 915 cm^{-1}, and 533 cm^{-1}) in the archaeological samples from Area I East and the heating experiment.

References

1. Ashton, N. M., Lewis, S. G. & Parfitt, S. A. *Excavations at Barnham, Suffolk, 1989-94*. (British Museum, 1998).
2. Fraile, J. & Calvo, M. Pseudomorphs: when the mineral is not what it was. *Mineral Up* **5**, 8–30 (2019).
3. Larkin, N. R. Pyrite decay: cause and effect, prevention and cure. *NatSCA News* **21**, 35–43 (2011).
4. Ashton et al. Handaxe and non-handaxe assemblages during Marine Isotope Stage 11 in northern Europe: recent investigations at Barnham, Suffolk, UK. *J. Quat Sci.* **31**, 837-843 (2016).
5. Kemp, R. A. in *Excavations at the Lower Palaeolithic Site at East Farm, Barnham, Suffolk, 1989-94* (eds Ashton, N.M., Lewis, S. G. & Parfitt, S.A.) 83-89 (British Museum, 1998).
6. Parfitt, S. A. in *Excavations at the Lower Palaeolithic Site at East Farm, Barnham, Suffolk, 1989-94* (eds Ashton, N. M., Lewis, S. G. & Parfitt, S. A.) 167-171 (British Museum, 1998).
7. Lewis, S. G. in *Excavations at the Lower Palaeolithic Site at East Farm, Barnham, Suffolk, 1989-94* (eds Ashton, N. M., Lewis, S. G. & Parfitt, S. A.) 23-78 (British Museum, 1998).
8. Preece, R. C. & Penkman, K. E. M. New faunal analyses and amino acid dating of the Lower Palaeolithic site at East Farm, Barnham, Suffolk. *Proc. Geol. Ass.* **116**, 363–377. (2005)
9. Voinchet P. et al. New chronological data (ESR and ESR/U-series) for the earliest Acheulian sites of north-western Europe. *J. Quat. Sci.* **30**, 610–622 (2015).
10. Parfitt, S. A. in *Excavations at the Lower Palaeolithic Site at East Farm, Barnham, Suffolk, 1989-94* (eds Ashton, N. M., Lewis, S. G. & Parfitt, S. A.) 111-147 (British Museum, 1998).
11. Hunt, C. O. in *Excavations at the Lower Palaeolithic Site at East Farm, Barnham, Suffolk, 1989-94* (eds Ashton, N. M., Lewis, S. G. & Parfitt, S. A.) 153-163 (British Museum, 1998).
12. Gale, S. J. & Hoare, P. G. *Quaternary Sediments: Petrographic Methods for the Study of Unlithified Rocks*. (Blackburn Press, 2011).
13. Bridgland, D. R. *Clast Lithological Analysis. Technical Guide No. 3.* (QRA, 1986).
14. Lewis, S. G. et al. A revised terrace stratigraphy and chronology for the early Middle Pleistocene Bytham River in the Breckland of East Anglia, UK. *Quat. Sci. Rev.* **269**, 107113 (2021).
15. Lewis, S. G., 1993. *The Status of the Wolstonian Glaciation in the English Midlands and East Anglia.* Unpublished PhD thesis, University of London.
16. Lewis, S. G. in *High Lodge. Excavations by G. de G. Sieveking (1962-68) and J. Cook (1988)* (eds Ashton, N. M., Cook, J., Lewis, S. G., Rose, J.), 51-86 (British Museum Press, 1998).
17. Ashton, N. M. et al. Excavations at the Lower Palaeolithic site at Elveden, Suffolk, UK. *Proc. Prehist. Soc.* **71**, 1–61 (2005).
18. Bridgland, D. R., Lewis, S. G. & Wymer, J. J. 1995. Middle Pleistocene stratigraphy and archaeology around Mildenhall and Icklingham, Suffolk. *Proc. Geol. Ass.* **106**, 57–69 (1995)
19. Davis, R.J. et al. A revised terrace stratigraphy and chronology for the Little Ouse River as a framework for interpreting the late Lower and early Middle Palaeolithic of central East Anglia, UK. *Quat. Environ & Humans* **2**, 100045 (2024).
20. Davis, R. J. et al. New evidence for the Clactonian-Acheulean succession during MIS 11 from Devereux's Pit, Suffolk, UK. *Quat. Sci. Rev*. (submitted).
21. Hunt, C. O. et al. *Central East Anglia and the Fen Basin. Field Guide*. 85-92. (QRA, 1991).
22. Mentzer, S. M. Microarchaeological approaches to the identification and interpretation of combustion features in prehistoric archaeological sites. *J. Archaeol. Meth. Theory* **21**, 616-668 (2014).
23. Goldberg, P., Miller, C. E. & Mentzer, S. M. Recognizing fire in the Paleolithic archaeological record. *Curr. Anthrop.* **58**, S16, S175-S190 (2017).
24. Thieme, H. in: *The hominid individual in context: archaeological investigations of Lower and Middle Palaeolithic landscapes, locales and artefacts* (eds Gamble, C. & Porr, M.) 115-132. (Routledge, 2005).
25. Gowlett, J. A. J. et al. Early archaeological sites, hominid remains and traces of fire from Chesowanja, Kenya. *Nature* **294**, 125–129 (1981).
26. Barbetti, M. Traces of fire in the archaeological record, before one million years ago? *J. Hum. Evol.* **15**, 771-781 (1986).
27. Stahlschmidt, M. C. et al. On the evidence for human use and control of fire at Schöningen. *J. Hum. Evol.* **89**, 181-201 (2015).

28. Hoare, S. et al. Living with fire: new micro contextual evidence for hearths from the Lower Palaeolithic site of Beeches Pit UK, MIS 11 (400 ka). *Nature Communications* (in review).
29. Stoops, G. *Guidelines for Analysis and Description of Soil and Regolith Thin Sections*. *Soil Sci. Soc. Am.* (Madison, 2003).
30. Stoops, G. *Guidelines for Analysis and Description of Soil and Regolith Thin Sections.* (Wiley, 2021).
31. Gualtieri, A. F. & Venturelli, P. In situ study of the goethite-hematite phase transformation by real time synchrotron powder diffraction. *Amer. Mineral.* **84**, 895–904 (1999).
32. Liu, Q. et al. Environmental magnetism: principles and applications. *Rev. Geophys.* **50**, 1-50 (2012).
33. Jordanova, D. et al. The role of tephra additions on development of incipient soils from Livingston Island (Antarctic Peninsula) revealed by environmental magnetism. Catena **212**, 106103 (2022).
34. Gedye, S. J. et al. The use of mineral magnetism in the reconstruction of fire history: a case study from Lago di Origlio, Swiss Alps. *Palaeogeog. Palaeoclim. Palaeoecol.* **164**, 101-110 (2000).
35. Dalan, R. A., & Banerjee, S. K. Solving archaeological problems using techniques of soil magnetism. *Geoarchaeol.: Internat. J.* **13**, 3-36 (1998).
36. Linford, N. T. & Canti, M. G. Geophysical evidence for fires in antiquity: preliminary results from an experimental study. Paper given at the EGS XXIV General Assembly in The Hague, April 1999. *Archaeol. Prospec.* **8**, 211-225 (2001).
37. Oldfield, F. & Crowther, J. Establishing fire incidence in temperate soils using magnetic measurements. *Palaeogeog. Palaeoclim. Palaeoecol.* **249,** 362-369 (2007)
38. Carrancho, Á. et al. Rock-magnetic analyses as a tool to investigate archaeological fired sediments: a case study of Mirador cave (Sierra de Atapuerca, Spain). *Geophys. J. Internat.* **179**, 79-96 (2009).
39. Herries, A. I., & Fisher, E. C. Multidimensional GIS modelling of magnetic mineralogy as a proxy for fire use and spatial patterning: Evidence from the Middle Stone Age bearing sea cave of Pinnacle Point 13B (Western Cape, South Africa). *J. Hum. Evol.* **59**, 306-320 (2010).
40. Lyons, R., Tooth, S., & Duller, G. A. Late Quaternary climatic changes revealed by luminescence dating, mineral magnetism and diffuse reflectance spectroscopy of river terrace palaeosols: a new form of geoproxy data for the southern African interior. *Quat. Sci. Rev.* **95**, 43-59 (2014).
41. Mullins, C. E. Magnetic susceptibility of the soil and its significance in soil science–a review. *J soil sci.* **28**, 223-246 (1977).
42. Rummery, T. A. et al. The persistence of fire-induced magnetic oxides in soils and lake sediments. *Annal Géophys.* **35**, 103–107 (1979).
43. Dearing, J. A. in *Environmental Magnetism: A Practical Guide*. (eds Walden, J., Oldfield, F. & Smith, J. P.) 25–62 (Quaternary Research Association, 1999).
44. Maher, B. A. The magnetic properties of some synthetic submicron magnetites. *Geophys. J. Roy. Astron. Soc.* **94**, 83–96 (1988).
45. Maki, D., Homburg, J. A., & Brosowske, S. D. Thermally activated mineralogical transformations in archaeological hearths: inversion from maghemite γFe2O4 phase to haematite αFe2O4 form. *Archaeolog. Prospec.* **13**, 207-227 (2006).
46. Herrejón Lagunilla, Á. et al. An experimental approach to the preservation potential of magnetic signatures in anthropogenic fires. *PLoS One* **14**, e0221592 (2019).
47. Sanz, M. et al. Early evidence of fire in south-western Europe: The Acheulean site of Gruta da Aroeira (Torres Novas, Portugal). *Sci. Rep.* **10**, 12053 (2020).
48. Thompson, R. & Oldfield, F. *Environmental Magnetism*. (Allen and Unwin, 1986).
49. Ketterings, Q. M., Bigham, J. M., & Laperche, V. Changes in soil mineralogy and texture caused by slash-and-burn fires in Sumatra, Indonesia. *Soil Sci. Soc. Am. J.* **64**, 1108-1117 (2000).
50. Pulley, S., Lagesse, J. & Ellery, W. The mineral magnetic signatures of fire in the Kromrivier wetland, South Africa. *J. Soils and Sed.* **17**, 1170-1181 (2017).
51. Walden, J., Oldfield, F. & Smith, J. P. (eds) *Environmental Magnetism: A Practical Guide* (QRA, 1999).
52. Worm, H. U. On the superparamagnetic—stable single domain transition for magnetite, and frequency dependence of susceptibility. *Geophys. J. Internat.* **133**, 201-206 (1988).
53. Blundell, A. et al. Controlling factors for the spatial variability of soil magnetic susceptibility across England and Wales. *Earth Sci. Rev.* **95**, 158-188 (2009)

54. Snape, L. & Church, M. J. Experimental magnetic susceptibility signatures for identifying hearths in the Mesolithic period in north east England, UK. *Wild Things 2.0: Further Advances in Palaeolithic and Mesolithic Research* 55-80 (2019).
55. Clark, A. *Seeing Beneath the Soil: Prospecting Methods in Archaeology*. (Batsford, 1996).
56. Karp, A. T. et al. Fire distinguishers: Refined interpretations of polycyclic aromatic hydrocarbons for paleo-applications. *Geochimica et Cosmochimica Acta* **289**, 93-113 (2020)
57. Song, Y. et al. Distribution of pyrolytic PAHs across the Triassic-Jurassic boundary in the Sichuan Basin, southwestern China: Evidence of wildfire outside the Central Atlantic Magmatic Province. *Earth Sci. Rev.* **201**, 102970 (2020).
58. Hytönen, K. et al. Gas–particle distribution of PAHs in wood combustion emission determined with annular denuders, filter, and polyurethane foam adsorbent. *Aerosol Sci. Tech.* **43**, 442-454 (2009).
59. McDonald, J. D. et al. Fine particle and gaseous emission rates from residential wood combustion. *Environ. Sci. Tech*. **34**, 2080-2091 (2000).
60. Aldeias, V. Experimental approaches to archaeological fire features and their behavioral relevance. *Curr. Anthrop.* **58(S16)**, S191-S205 (2017).
61. Hoare, S. Assessing the function of Palaeolithic hearths: experiments on intensity of luminosity and radiative heat outputs from different fuel sources. *J. Paleol. Archaeol.* **3**, 537-565 (2020).
62. Argiriadis, E. et al. Lake sediment fecal and biomass burning biomarkers provide direct evidence for prehistoric human-lit fires in New Zealand. *Sci. Rep.* **8**, 12113 (2018).
63. Campos, I. & Abrantes, N. Forest fires as drivers of contamination of polycyclic aromatic hydrocarbons to the terrestrial and aquatic ecosystems. Curr. Opin. *Environ. Sci. Health* **24**, 100293 (2021).
64. Denis, E. H. et al. Polycyclic aromatic hydrocarbons (PAHs) in lake sediments record historic fire events: Validation using HPLC-fluorescence detection. *Org. Geochem.* **45**, 7-17 (2012).
65. Brittingham, A. et al. Geochemical evidence for the control of fire by Middle Palaeolithic hominins. *Sci. Rep.* **9**, 15368 (2019).
66. Sojinu, O. S., Sonibare, O. O. & Zeng, E. Y. Concentrations of polycyclic aromatic hydrocarbons in soils of a mangrove forest affected by forest fire. *Toxicolog. Environ. Chem.* **93**, 450-461 (2011).
67. Yunker, M. B. et al. PAHs in the Fraser River basin: a critical appraisal of PAH ratios as indicators of PAH source and composition. *Org. Geochem.* **33**, 489-515. (2002).
68. Faboya, O. L. et al. Impact of forest fires on polycyclic aromatic hydrocarbon concentrations and stable carbon isotope compositions in burnt soils from tropical forest, *Nigerian Sci. Afr.* **8**, e00331 (2020).
69. Lerario, V. L. et al. Sources and distribution of polycyclic aromatic hydrocarbons (PAHs) in sediments from the Mar Piccolo of Taranto, Ionian Sea, southern Italy. *Annali di chimica* 93, 397-406. (2003).
70. Sprovieri, M. et al. Heavy metals, polycyclic aromatic hydrocarbons and polychlorinated biphenyls in surface sediments of the Naples harbour (southern Italy). *Chemosphere* 67, 998-1009 (2007).
71. Fine, P. M., Cass, G. R. & Simoneit, B. R. Chemical characterization of fine particle emissions from the fireplace combustion of woods grown in the southern United States. *Envir. Sci. Tech.* **36**, 1442-1451 (2002).
72. Fine, P. M., Cass, G. R. & Simoneit, B. R. Chemical characterization of fine particle emissions from the fireplace combustion of wood types grown in the Midwestern and Western United States. *Envir. Engin. Sci.* **21**, 387-409 (2004a).
73. Fine, P. M., Cass, G. R. & Simoneit, B. R. Chemical characterization of fine particle emissions from the wood stove combustion of prevalent United States tree species. *Envir. Engin. Sci.* **21**, 705-721 (2004b)
74. Madejova, J. & Komadel, P. Baseline studies of the Clay Mineral Society source clays: Infrared methods. *Clays and Clay Minerals* **49**, 410-432 (2001).
75. Berna, F. et al. Sediments exposed to high temperatures: reconstructing pyrotechnological processes in late bronze and iron age strata at Tel dor (Israel). *J. Archaeol. Sci.* **34**, 358-373 (2007).
76. Saikia, B. J. & Parthasarathy, G. 2010. Fourier Transform Infrared Spectroscopic characterization of kaolinite from Assam and Meghalaya, Northeastern India. *J. Mod. Phys.* **1**, 206-210 (2010).
77. FTIR reference collection, Kimmel Center of Archaeological Science, Weizmann Institute of Science, http://www.weizmann.ac.il/kimmel-arch/infrared-spectra-library.mel-arch/infrared-spectra-library.
78. Ogloblin Ramirez, I. et al. Infrared spectra of mixtures of heated and unheated clay: Solving an interpretational conundrum. *Geoarchaeol.* **38**, 822-829. (2023).